Research Square

Preprints are preliminary reports that have not undergone peer review.
They should not be considered conclusive, used to inform clinical practice,
or referenced by the media as validated information.

Extending Axiomatic Design: A Dual-Domain Mapping Framework for Complete Physical Architecture — Co-Generating Functional and Decoupling Components

Jinping Li

1563672832@qq.com

Southwest Jiaotong University

Guofu Ding

Southwest Jiaotong University

Research Article

Keywords: Co-generation of decoupling components, Functional-to-physical mapping, Implicit coupling, Complex network analysis, Physical architecture design

Posted Date: November 17th, 2026

DOI: https://doi.org/10.21203/rs.3.rs-11436685/v1

License: This work is licensed under a Creative Commons Attribution 4.0 International License.
Read Full License

Additional Declarations: No competing interests reported.

Extending Axiomatic Design: A Dual-Domain Mapping Framework for Complete Physical Architecture — Co-Generating Functional and Decoupling Components

Jinping Li [a, *] (Corresponding author), Email: 1563672832@qq.com, Guofu Ding[a]
[a] Institute of Advanced Design and Manufacturing, Southwest Jiaotong University, Chengdu 610031, P.R.China

Abstract: This paper extends Axiomatic Design (AD) to address a fundamental design problem in physical architecture synthesis: functional-centric mapping fails to characterize physical field coupling, and decoupling components lack representation within the existing framework. The core scientific question is: **Does functional independence imply physical independence?** If not, what representational extensions are required for function-centric design theory to characterize physical field coupling and enabling the **systematic recommendation** of decoupling components? Existing theories—AD, FBS, TRIZ, and DSM—assume that a valid physical architecture can be obtained whenever functional decomposition is correct and compatibility constraints are satisfied. However, this assumption is incomplete: functionally independent components can still become coupled through shared physical fields, resulting in degraded product performance and quality. Furthermore, **decoupling components**—elements that implement no functional requirements but serve to suppress physical field coupling—cannot be represented. Consequently, existing theories can only generate functional components and cannot guide the creation of decoupling components, rendering the resulting physical architecture incomplete. Upon integration, problems such as vibration, noise, electromagnetic interference, and thermal failure frequently necessitate iterative redesign and can even precipitate safety incidents. To bridge this gap, this paper proposes a **dual-domain extension of Axiomatic Design** that places physical field interactions and functional logic on equal theoretical footing. The framework integrates residual coupling networks, latent coupling inference, coupling elasticity matrices, positive feedback loop detection, and P0–P3 priority ranking with Constraint Satisfaction Problem (CSP) filtering, Graph Neural Network (GNN) surrogate models, and Pareto optimization. In a high-speed train case study, 2,187 candidate combinations are filtered down to 468 feasible architectures. Scheme 261 (Ω=1) theoretically achieves suppression rates of **93.2% (implicit)** and **74.1% (boundary)**. Type I validation and Type II confirmation—including external consistency with published measurement data, retrospective analysis of industrial cases, and sensitivity analysis—substantiate the theoretical merit and **plausibility** of the proposed extension.

Keywords: Co-generation of decoupling components; Functional-to-physical mapping; Implicit coupling; Complex network analysis; Physical architecture design

1 Introduction

This paper extends Axiomatic Design (AD) to address a fundamental problem in physical architecture **synthesis** of complex electromechanical systems: **how to represent and manage couplings that arise when functionally independent components interact through shared physical fields**—such as vibration, electromagnetic interference, thermal flux, and acoustic propagation—thereby enabling the synthesis of necessary decoupling components and generating a complete physical architecture that satisfies product performance and quality requirements.

The underlying scientific question is: **Does functional independence necessarily imply physical independence?** If not, what representational extensions must function-centric design theory undergo to characterize physical field coupling and enable the systematic generation of decoupling components?

Existing frameworks—AD, FBS, TRIZ, and DSM—rest upon a shared premise: provided that functional decomposition is sound and compatibility constraints are satisfied, a valid physical architecture will result. This assumption, however, is incomplete. Moreover, among these frameworks, AD is **among the most rigorous and axiomatically grounded**, offering a clear entry point for the required theoretical extension.To address this gap, this paper proposes a **dual-domain extension of AD** that accords functional and physical field domains equal representational status.

AD's Independence Axiom stipulates that each Functional Requirement (FR) be controlled by a unique Design Parameter (DP), yielding a diagonal or triangular design matrix. This formalizes the ideal of functional independence and provides a rigorous criterion for conceptual validity. Yet the design matrix characterizes *functional dependencies*—the sensitivity of FR to variations in DP—and imposes no constraints on material properties, geometric configuration, or boundary conditions. Functionally independent components can nevertheless become coupled via shared physical fields; many such couplings degrade product performance and quality below acceptable design specifications. Addressing these requirements necessitates the introduction of dedicated **decoupling components**.

Decoupling components implement no functional requirements; their sole role is to suppress physical field coupling. Critically, **within AD—as within FBS, TRIZ, and DSM—decoupling components lack any formal representation or generation mechanism**.

This representational gap carries immediate and severe consequences: **existing theories can only synthesize functional components and provide no guidance for the generation of decoupling components; the resulting physical architecture is therefore incomplete.** Upon system integration, problems—vibration, noise, electromagnetic interference, and thermal failure—emerge, rendering product performance and quality difficult to achieve, necessitating iterative redesign and occasionally precipitating safety failures. Consequently, function-centric design theory alone is insufficient to support the synthesis of a complete physical architecture. **What is required is a representational extension capable of simultaneously capturing functional logic and physical field coupling**, thereby enabling the systematic generation of decoupling components, forming a complete physical architecture, and ensuring that product performance and quality meet specification.

The physical architecture of a complex system defines its constituent modules and their interconnection topology. Consequently, architecture design methodology determines not only the degree to which functional objectives are realized but also whether the integrated system can operate reliably under realistic physical conditions. Model-Based Systems Engineering (MBSE) provides systematic approaches to requirements management and multi-view consistency throughout the design process [5]; however, it does not explicitly address the physical field interactions that arise from module coexistence.

Most function–physical mapping frameworks—whether Functional–Behavioral–Structural (FBS) [10–12], TRIZ [13, 14], or Axiomatic Design (AD) [28–34]—rest upon a fundamental assumption: if functional requirements are correctly decomposed and mapped to physical components that implement them, the resulting architecture will be valid. This paper argues that this assumption is **inherently incomplete.**

Consider a high-speed train. The car body and bogie are functionally independent: the car body provides passenger accommodation; the bogie delivers propulsion capability. Yet upon integration, wheel–rail excitation propagates through the suspension interface into the car body, inducing vibration and interior noise. Simultaneously, equipment mounted beneath the car body—such as traction transformers, power converters, and braking resistors—generate vibration during operation; this vibration is transmitted through mounting brackets to the car body, directly causing localized vibration and degrading ride comfort while exciting radiating structural modes that produce airborne noise. This exemplifies a **paradigmatic instance of implicit coupling**: the equipment vibration and car body are functionally independent, yet become coupled through spatial co-location within a shared physical field (vibratory). Critically, this relationship is never formally documented in the design interface.

Analogously, the traction power converter and network control system belong to distinct functional domains—power and control, respectively—yet incur electromagnetic field coupling due to spatial proximity. Similarly, the thermal–mechanical coupling within brake disks is stipulated by no functional requirement. Like the equipment vibration described above, these interactions constitute **physical field couplings unrepresented in functional decomposition**; despite their disparate coupling mechanisms and propagation physics, they remain architecturally invisible.

This phenomenon is far from unique to rail transit. In aerospace engineering, the POGO oscillation encountered during the Shenzhou-5 mission provides a particularly instructive example. In 2003, China's first astronaut Yang Liwei ascended aboard Shenzhou-5; during the 120–140 second flight interval, he experienced severe vibration that he later described as extremely painful and progressively worsening. Post-flight analysis confirmed the cause: **POGO oscillation**—longitudinal coupling between the launch vehicle's structural dynamics and propellant supply system pressure oscillations 35. The vibration frequency, approximately 8 Hz, coincided closely with the human cardiac fundamental frequency, posing direct physiological risk to the astronaut.

The response within the Shenzhou program reveals two distinct levels of intervention. During Shenzhou-6, the engineering team reduced the number of bellows accumulators in the booster from two to one—a **parameter-level adjustment** to an existing decoupling device that measurably attenuated vibration amplitude and duration. This intervention was fundamentally a parametric patch: the residual coupling matrix was weakened, yet the underlying coupling mechanism remained intact. During Shenzhou-7, the team replaced the conventional accumulator with a **variable-volume accumulator** that exhibits pressure–volume characteristics adaptive to different flight phases, thereby absorbing propellant oscillation energy and detuning the supply system's natural frequency away from structural resonance conditions. Consequently, POGO oscillation was **effectively eliminated in that mission**. Notably, the variable-volume accumulator itself implements *no functional requirement*; its sole purpose is to suppress the physical field coupling between two functionally independent subsystems—rendering it a **clear example** of a decoupling component as a second-order design object.

Automotive engineering further demonstrates that such decoupling components are not merely theoretical constructs but constitute mature industrial practice. The second-generation magnetorheological powertrain mount developed by BWI Group for the 2017 Mercedes-AMG E 63 S integrates a decoupling system that establishes a secondary fluid flow path on demand to reduce

mount stiffness. Whereas the first-generation mount addressed large transient events in the 2–22 Hz bandwidth, the second-generation design extends vibration isolation to small-amplitude motions in the 30–150 Hz range, thereby simultaneously addressing low-frequency powertrain motion control and high-frequency noise attenuation. This decoupler is *not* a functional component of the powertrain; rather, it is a **dedicated coupling suppression device embedded within the mount architecture.** In chassis design, BMW's dual-ball-joint front suspension resolves the lower control arm into two independent links connected to the subframe via hydraulic bushings, thereby decoupling longitudinal and lateral wheel forces while isolating suspension dynamics from the vehicle body. The hydraulic bushing equally constitutes a **decoupling component**: its purpose is not to realize any functional requirement of the steering or suspension systems, but rather to suppress the transmission of physical disturbance originating from the tire–road interface.

These engineering cases share a common structural pattern: **functionally independent subsystems become coupled through physical fields—vibration, pressure oscillation, mechanical force transmission—that functional decomposition cannot represent; the resulting solutions are in every instance not functional components but dedicated decoupling components**—variable-volume accumulators, magnetorheological decouplers, hydraulic bushings. Critically, **none of these decoupling components were introduced proactively during architecture design; instead, they were all introduced *post hoc*, after coupling problems had manifested**—through astronaut physiological distress, through vehicle NVH measurement, through field observation. Engineering practice repeatedly demonstrates that decoupling components are indispensable; what existing design theory lacks is not awareness of the need for such components, but rather **a representational mechanism that enables them to be generated as constitutive elements within the architecture design process, rather than introduced as post-hoc remedial measures.**

The four frameworks share a common function-centric assumption; the gap is not four independent deficiencies but rather **four manifestations of a single representational lacuna.** Specifically, the critical representational element lacking in each framework is as follows.

Functional–Behavioral–Structural (FBS) Framework lacks a representational dimension for **physical fields.** The three-layer FBS architecture—function, behavior, structure—defines behavior as the mechanism by which structure realizes function. This enables FBS to represent statements such as "the car body realizes passenger accommodation" or "the bogie realizes propulsion capability," yet it cannot represent the **physical field propagation process**: "bogie vibration propagates into the car body through the suspension interface." Consequently, the implicit coupling whereby equipment vibration is transmitted to the car body through mounting brackets has no corresponding representational object within FBS; the designer cannot identify it during functional decomposition.

Theory of Inventive Problem Solving (TRIZ) lacks a representational dimension for **non-parametric field coupling.** TRIZ identifies and resolves technical contradictions through contradiction matrices, with functional parameters as input—for example, "improve vibration isolation *vs.* increase mass." However, POGO oscillation and NVH coupling do not manifest as contradictions between functional parameters; they fundamentally do not appear in functional parameter space. Consequently, TRIZ's contradiction matrix cannot capture such couplings, nor can it derive decoupling components—such as variable-volume accumulators—through contradiction resolution.

Axiomatic Design (AD) lacks a representational location for **components that implement no functional requirement.** The AD design matrix employs functional requirements (FRs) as rows and design parameters (DPs) as columns. Variable-volume accumulators, magnetorheological decouplers, and hydraulic bushings implement *no* functional requirement; consequently, they correspond to neither any FR row nor any DP column. Within AD's representational framework, such second-order design objects cannot be represented at all. This means that even if the design matrix satisfies the Independence Axiom, the system may still fail due to physical field coupling—**AD provides no guarantee that field coupling strength $\Psi_{ij} = 0$.**

Design Structure Matrix (DSM) lacks a representational distinction between **functional dependency and physical field coupling,** and it lacks a mechanism to derive decoupling requirements from functional requirements. DSM describes design dependencies among components, yet conflates interfaces, signal flows, energy flows, and physical field couplings into a single undifferentiated matrix. More critically, **DSM's input is a predetermined set of components; it does not generate new components.** Therefore, DSM cannot derive the conclusion "a decoupling component is required here" from functional requirements.

Precisely because each of these four theories lacks the representational elements specified above, the physical architecture generation process is **structurally deficient in necessary decoupling components.** This consequence manifests in engineering

practice as: **decoupling components can only be introduced post-hoc, after problems have manifested**—the reduction in bellows accumulator count in Shenzhou-6 constitutes a parametric patch, until Shenzhou-7 achieved mechanism-level decoupling through the variable-volume accumulator; similarly, AMG's magnetorheological decoupler and BMW's hydraulic bushing are both remedial responses to NVH problems that had already emerged.

Therefore, the core problem shifts from **"how to optimize known couplings"** to **"how to discover couplings that have been observed but remain incompletely understood, predict potential couplings that have not yet been discovered, issue early warnings for high-risk pathways, and generate design objects that suppress implicit and boundary couplings—while preserving explicit couplings as hard constraints."** This shift is not merely a change in terminology; it constitutes **a significant redefinition** of the design problem itself.

The framework of "optimizing known couplings" tacitly presupposes that couplings have already been identified, documented, and parameterized. However, engineering practice repeatedly demonstrates that this premise does not hold. What truly causes integration failure, rework cycles, and even safety accidents is not the couplings already documented, but rather two classes of **"off-the-books" couplings.** The first class comprises couplings that have been observed but remain incompletely understood: they exist physically, their manifestations have surfaced, yet their mechanisms, propagation pathways, and consequences remain insufficiently comprehended—the frequency coupling between the propulsion and structural systems in the Shenzhou-5 POGO oscillation event exemplifies this category. This coupling existed during the design phase, yet revealed itself only in flight; its underlying mechanisms were subsequently understood only through iterative post-flight analysis. The second class comprises potential couplings that have not yet been discovered: although unconfirmed, their possible existence can be inferred from network topology and physical field overlap—the twenty high-risk pathways inferred from L1.5 layer analysis exemplify this category. If the problem is framed as "optimize known couplings," both classes of couplings lie entirely outside the optimization objective set from the outset. No matter how well the optimization is executed, it can only cover a subset of all couplings. **This is the fundamental limitation of the "optimize known couplings" paradigm: it defines the design problem within the space of known couplings, while actual failures occur precisely outside this space.**

Therefore, the problem must be correspondingly redefined. **Discovering couplings that have been observed but remain incompletely understood** means inferring, during the design phase, those coupling pathways that are physically present but still incompletely comprehended, based on the record of known couplings—the Shenzhou-5 POGO oscillation serves as a canonical example: the coupling between propulsion and structural systems existed during design, yet revealed itself only in flight, and its underlying mechanisms remain incompletely understood even thereafter. **Predicting potential couplings that have not yet been discovered** means inferring, during the architecture generation phase, coupling pathways that remain unconfirmed—this is precisely the mission of the L1.5 potential coupling inference layer, which, based on network topology similarity, physical field overlap, and subsystem membership, infers unknown couplings from known couplings, thereby **potentially enabling** designers to transition from **"post-hoc response"** to **"ex-ante warning." Issuing early warnings for high-risk pathways** means no longer waiting until all couplings have manifested before addressing them individually, but rather prioritizing coupling pathways during the architecture generation phase, concentrating design resources on P0/P1 high-risk pathways.

Generating design objects that suppress implicit and boundary couplings means that decoupling components should be proactively constructed as candidate design objects during the architecture synthesis phase. **Preserving explicit couplings as hard constraints** means that physical connections critical to system functional realization—bolts, wire harnesses, signal interfaces—are not forcibly decoupled, but rather enter the optimization process as immutable constraints.

This redefinition is precisely the point of departure for the dual-domain mapping framework. The so-called "dual domains" refer to the functional domain and the physical field domain being positioned as equivalent representational structures, rather than treating the functional domain as the sole organizational backbone. The functional domain answers "what functional components constitute the system, and how do they realize functional requirements?"; the physical field domain answers "what physical field interactions arise when these components coexist, how do coupling pathways propagate, which couplings require suppression, and by what decoupling components are they suppressed?" The two domains operate in parallel throughout the entire architecture generation process: the functional domain generates candidate functional components through FBS-TRIZ mapping, while the physical field domain identifies explicit, implicit, and boundary couplings via residual coupling matrices, diagnoses coupling pathways using complex network analysis and **coupling elasticity matrix**, and reveals coupling paths that **may exist** but have not been documented through L1.5 potential coupling inference, predicting couplings that remain unconfirmed.

On this foundation, decoupling components are no longer introduced as post-hoc remedial measures after integration problems emerge; rather, they are jointly represented, jointly generated, jointly evaluated, and jointly decided upon with functional components in the same design space. Joint representation means that decoupling components and functional components possess equally explicit design object status; joint generation means that decoupling solutions are triggered and constructed during the architecture synthesis phase itself; joint evaluation means that residual couplings are incorporated into multi-objective assessment alongside performance metrics; joint decision-making means that decoupling priorities and architecture choices are resolved within a single unified decision framework.

The theoretical foundation of this framework is precisely Theorem 1, the incompleteness theorem of functional-physical mapping: functional independence does not entail physical independence; physical field interactions in spatially extended systems cannot be completely encoded by functional logic. Therefore, dual-domain mapping is not a localized patch to existing design theory, but rather **a structural extension of Axiomatic Design's representational scheme**—it transforms decoupling from post-hoc remediation based on engineering intuition into an intrinsic constituent of architecture design.

Existing methods can be classified into three categories, all of which fail to address the problem of decoupling component generation. Rule-based configuration methods [1,3,4,6] and intelligent design exploration methods 2 presuppose that compatibility constraints suffice to capture physical interactions; simulation-based evaluation methods [7,22] require complete system models, whereas implicit couplings are by definition those that escape representation in such models; domain integration frameworks [8,9] recognize that the functional and physical domains are inseparable, yet provide no mechanism for generating countermeasures. All these methods operate under the same fundamental assumption: given functional components and compatibility rules, effective architecture will automatically emerge. In fact, the rules and constraints themselves employed by these methods constitute a symptomatic acknowledgment—"components will interfere with one another"—yet implicit couplings have never been treated as first-class design concepts requiring explicit representation and systematic mitigation.

Pradas Gómez et al. [8] directly challenge the sequential processing of the functional and physical domains, demonstrating their inseparability in design space exploration. FUSE [9] provides a pragmatic response, combining enriched functional models with automated physical parameter sampling. However, despite these works acknowledging the existence of cross-domain interactions, they still fail to provide a systematic representational scheme for coupling interactions: they neither distinguish coupling types (explicit, implicit, boundary), nor characterize their propagation pathways, nor establish a mechanism to match feasible decoupling strategies to specific coupling types. More critically, they provide no method for systematically generating decoupling components as intrinsic constituents of architecture synthesis, but instead continue to treat decoupling as a post-hoc remedial measure. Furthermore, neither of these works addresses residual coupling quantification, potential coupling inference, or early warning of high-risk pathways, and therefore cannot support the transition from "identifying interactions" to "generating decoupling components."

To bridge this gap, this paper proposes a **dual-domain mapping framework**, whose core insight is that traditional functional-structural mapping treats physicality as a **mere carrier of function.** In this one-dimensional mapping, functional components constitute the sole output, while physical field interactions are either simplified away, ignored, or demoted to post-hoc constraint checking. However, physical interactions such as vibration, thermal effects, and electromagnetic interference do not vanish when two components are functionally independent. To overcome this limitation, the proposed framework **elevates physical field interactions to a knowledge dimension coequal with functional logic.** Thus, the design process simultaneously addresses two problems: **(1) mapping functional requirements to physical components, thereby generating the set of functional components C_{func}; and (2) analyzing physical disturbances arising when functional components coexist, thereby generating the set of decoupling components C_{dec} that suppress these disturbances.** The two domains operate synergistically throughout the entire architecture generation process, enabling functional and decoupling components to be **co-generated** rather than treating decoupling as post-hoc remediation. This is precisely what traditional functional-physical mapping cannot achieve, and is the direct consequence of the incompleteness revealed by Theorem 1.

Based on this insight, the framework unfolds as follows. The **functional domain** generates candidate functional components via FBS-TRIZ mapping, while the **physical field domain** constructs the system's coupling network through a sequential six-layer analysis **L0–L5. L0** defines functional components and boundary nodes, annotating their associated physical field types. **L1** performs first-order quantification of explicit, implicit, and boundary couplings, constructing the residual coupling matrix **R. L1.5** infers, based on network topology similarity, physical field overlap, and subsystem attribution, coupling paths that **may exist** but have not been documented, as well as potential couplings not yet discovered. **L2** constructs the **coupling elasticity matrix** to capture

higher-order interactions among coupling pathways, defines the pathway degree metric, and detects positive feedback loops. **L3** forms the system-level coupling network representation. **L4** synthesizes residual strength, pathway degree, and positive feedback loop risk, assigning priority labels **P0–P3. L5** matches decoupling strategies to priority tiers and coupling types, generating recommended decoupling components. Throughout this process, **constraint satisfaction problem (CSP)-based hard constraint screening** filters infeasible architectures, **graph neural network (GNN) surrogate models** rapidly predict seven performance indicators, and **residual coupling serves as an explicit metric of decoupling effectiveness.**

The proposed framework grounds coupling analysis in **complex network theory.** Coupling relationships are fundamentally bidirectional, and thus naturally represented as **undirected weighted graphs**, where nodes represent functional components and boundary nodes, edges represent coupling relationships, and edge weights are quantified by the residual coupling matrix. Based on this representation, **higher-order interaction analysis**, pathway degree quantification, and positive feedback loop detection jointly provide the basis for ordering decoupling objectives and are annotated with P0–P3 priority labels.

All decisions are **traceable to explicit mathematical criteria**, enabling designers to understand the reasoning chain behind each recommendation without reliance on black-box models.

The framework revolves around four research questions:

(RQ1) Representation and Generation: How can decoupling components and functional components be jointly represented and generated within a unified physical architecture design process, rather than being remedied only after integration problems emerge? **(RQ2) Rapid Multi-Objective Evaluation:** How can large-scale candidate architectures containing both functional and decoupling components be rapidly evaluated across multiple performance indicators without reliance on expensive high-fidelity simulation? **(RQ3) Network-Based Pathway Prioritization:** How can complex network analysis be leveraged to prioritize coupling pathways, thereby guiding decoupling intervention? **(RQ4) Internal Consistency and Validation:** How can the proposed framework be verified and validated through proof-of-concept demonstration, external consistency checks, sensitivity analysis, and falsifiable predictions, without recourse to hardware experimentation?

The principal contributions of this work are as follows:

(1) Theoretical Contribution: Representational Extension of Axiomatic Design. This paper proves that the Independence Axiom is a necessary but not sufficient condition for system integrability, and that AD lacks representational provisions for physical field couplings and components that realize no functional requirement. **Theorem 1 formalizes this representational incompleteness.** (Addresses RQ1 and RQ4)

(2) Methodological Contribution: Dual-Domain Extension of AD. This paper treats physical field interactions as an independent knowledge dimension coequal with functional logic, enabling functional and decoupling components to be jointly represented, evaluated, and ranked as equal design objects. The core is a **complete analytical chain from coupling modeling to decoupling decision support:** residual coupling matrix, **coupling elasticity matrix**, pathway degree, positive feedback loop detection, and P0–P3 priority assignment. **All decisions are traceable to explicit mathematical criteria.** Graph neural networks serve as auxiliary computational tools for rapid evaluation, not as the theoretical core of the framework. (Addresses RQ1 and RQ3)

(3) Computational Demonstration: High-Speed Rail Architecture Consistent with Operating Systems. The framework is demonstrated end-to-end on a 67-node architecture: CSP filtering reduces 2,187 candidate combinations to 468 feasible architectures; Pareto optimization selects Solution 261; the coupling network comprises 67 nodes and 90 edges; L1.5 inference identifies 20 high-risk potential coupling pathways; under assumed decoupling efficiency, theoretical suppression rates for implicit and boundary couplings are **93.2%** and **74.1%**, respectively. This demonstration is **illustrative, not an industrial validation.** (Addresses RQ2)

(4) Verification and Validation. Verification ensures the framework operates as specified, including code reproducibility, analytical cross-checks, numerical stability testing, enumeration correctness, and degenerate case handling. Validation demonstrates that the framework solves the intended design problem through: proof-of-concept demonstration, external consistency checks against published bench-test and field measurement data, **retrospective consistency checks** against documented industrial cases, sensitivity analysis of critical parameters, and a list of falsifiable predictions. Additionally, qualitative comparisons are provided against DSM, AD, rule-based configuration, pure simulation, and linear regression. (Addresses RQ4)

The remainder of this paper is organized as follows. **Section 2** surveys related work; **Section 3** introduces the methodology; **Section 4** presents the high-speed rail case study; **Section 5** reports verification and validation; **Section 6** discusses results and limitations; **Section 7** concludes.

2 Related Work

This section reviews the literature relevant to the proposed dual-domain extension of Axiomatic Design (AD). Section 2.1 examines how function-centric design theories—AD, FBS, TRIZ, and DSM—treat physical-field coupling, and identifies the representational gap that motivates this extension. AD is the primary focus because its Independence Axiom is the most formalized

and the most directly challenged by physical-field coupling. Sections 2.2 and 2.3 review multi-objective evaluation and complex-network methods, respectively, which provide the methodological foundation for the proposed framework.

2.1 Function-to-Physical Mapping and the Missing Decoupling Problem

2.1.1 The FBS-TRIZ Paradigm and Its Assumption

Function-Behavior-Structure (FBS) theory [10-12] provides the classical framework for mapping functional requirements to physical components. In FBS, designers decompose requirements through a "function → behavior → structure" hierarchy, where functional specifications are progressively transformed into structural forms. TRIZ [13,14] is often integrated with FBS to resolve technical contradictions that arise during this mapping process.

The classical FBS framework was established by Gero [10] and later extended to situated design by Gero and Kannengiesser [11], with critical analyses further refining its theoretical foundations [12]. More recent extensions incorporate agent-based reasoning [19], SysML extensions for mechatronic architecture modeling [20], skeleton model evaluation through FBS association analysis [18], and safety-oriented design approaches based on Product-Service Systems and FBS [16].

Despite these advances, all FBS-TRIZ approaches share a common structural assumption: **if functional decomposition is correct and all compatibility constraints are satisfied, the resulting physical architecture is valid** [10,11,15]. Within this assumption, the designer's task is to generate functional components—parts that directly realize specified functions—and then ensure their coexistence through rules.

The theoretical problem is this: the validity of coexistence is treated as a constraint satisfaction problem over the output of FBS mapping. The mapping itself generates only functional components; compatibility rules are added externally to prevent interference. But this formulation provides no mechanism for generating components whose *primary purpose* is to suppress interference—isolators, shields, compensators, buffers. The FBS paradigm has no representational slot for "a component that does not realize a function but enables other components to realize their functions without interference."

2.1.2 Axiomatic Design and the Boundary of the Independence Axiom

Axiomatic Design (AD) [28-34] advances coupling management from empirical practice to principle-driven discipline. Its Independence Axiom requires that each Functional Requirement (FR) be controlled by one Design Parameter (DP), producing a diagonal or triangular design matrix. This formalizes the ideal of functional independence and provides a rigorous criterion for conceptual soundness.

Numerous studies have extended AD across engineering domains, as reviewed in comprehensive surveys [28], with specific applications including case-based reasoning for knowledge graph construction [29], hybrid tractor design [30], supplier selection [31], ship design [32], and conceptual design [33,34].

However, AD's formulation has a scope boundary that is often overlooked. The design matrix captures **functional dependencies**—the sensitivity of FRs to changes in DPs. Implicit couplings of the kind this paper addresses (vibration transmission, EMI, thermal-mechanical coupling) arise not from FR–DP relationships but from shared physical fields, spatial coexistence, and propagation pathways. Two components can be axiomatically independent—their design matrix diagonal—yet strongly coupled in reality because their physical fields overlap. The Independence Axiom is necessary but not sufficient for system integrability.

The critical insight is this: AD does not generate decoupling components because its representational scheme has no place for them. The design matrix describes the relationship between FRs and DPs; decoupling components serve no direct FR. They are "second-order" components—their function is to enable the system to realize its FRs, not to realize any FR themselves. AD provides no theoretical basis for representing, let alone generating, such second-order components.

AD provides no theoretical basis for representing, let alone generating, such second-order components.

2.1.3 The Root Problem: A Missing Representational Slot in Function-Centric Design Theories

Across FBS, TRIZ, and AD, the same structural gap recurs: the representation of functional logic and physical reality is one-dimensional. The mapping takes functions as input and outputs structural forms that realize those functions. Physical-field interactions—vibration, EMI, thermal, acoustic—are treated as external constraints to be managed after the fact, rather than as first-class design entities requiring explicit representation and systematic mitigation.

This explains why configuration rules and constraints are necessary in practice: they are symptomatic acknowledgments that the underlying mapping is incomplete. Configuration rules and constraints serve as heuristic compensations for the mapping's inability to recognize that physically coexisting modules will interfere. They are not design principles but patches for a structurally incomplete representation [37-38].

Our previous work [39] empirically demonstrated this incompleteness in the context of high-speed train modularization, revealing that residual implicit couplings still exist after DSM-driven partitioning. That study developed a "decouple-first, partition-second" static modular partitioning framework built upon the residual coupling matrix, which operates on a fixed set of components to derive module boundaries. Nevertheless, it stays strictly within the partitioning paradigm and cannot produce multiple alternative architectures or perform architecture selection.

Different from such static partitioning, this paper focuses on physical architecture synthesis: we aim to co-generate functional and decoupling components starting from design requirements, introduce a **coupling elasticity matrix** for higher-order coupling diagnosis, and adopt the CSP-GNN-Pareto pipeline to screen and rank massive candidate architectures. This paper bridges the above-mentioned research gap. While this gap is shared by FBS, TRIZ, and DSM, it is most consequential for AD because AD explicitly claims that satisfying the Independence Axiom yields a valid architecture. Extending AD therefore offers the most direct route to closing this gap.

2.2 Multi-Objective Evaluation: Limitations for Architectures with Decoupling Components

After architectures are generated, they must be evaluated. The evaluation literature has developed sophisticated methods, yet these methods share assumptions that become problematic when architectures include decoupling components.

2.2.1 Three Categories of Evaluation Methods

Simulation-based evaluation uses bond graphs or multi-body dynamics to derive quantitative performance metrics [7]. While precise, it requires a complete system model—including all interaction paths—before simulation. Implicit couplings are, by definition, absent from the initial model topology. The method cannot evaluate what it cannot represent.

Multi-attribute decision-making methods [21-27] handle qualitative indicators, uncertainty, and expert disagreement through frameworks such as AHP-fuzzy evaluation [23], rough-Z-number MCGDM [24], prospect theory [25], TOPSIS [1], and VIKOR [7]. These methods have progressively addressed psychological bias and information reliability. However, they assume evaluation criteria and weights are fixed in advance. Decoupling components, by design, alter the coupling structure of the system; their inclusion changes the relative importance of performance criteria. A static weighting scheme cannot capture this dynamic trade-off.

Pareto-based multi-objective optimization [22] avoids a priori weighting by identifying non-dominated frontiers. When scaled to architectures with decoupling components, however, the combinatorial explosion of candidates makes high-fidelity evaluation computationally prohibitive for every combination.

2.2.2 Common Limitation: Static Assumptions

These methods share a common limitation: they evaluate architectures *after* they are generated, assuming the set of candidates is already complete. None provides feedback to the generation process about whether the candidate set *itself* is structurally complete—i.e., whether all necessary decoupling components have been included.

The implication for this paper: evaluation of architectures with decoupling components requires (i) a metric that explicitly quantifies decoupling effectiveness (residual coupling), (ii) a surrogate model that enables rapid evaluation across combinatorially expanded candidate sets, and (iii) a dynamic weighting scheme that can reflect the coupling-altering effect of decoupling interventions. Section 3 addresses these requirements.

2.3 Application of Complex Networks in Coupling Analysis

Complex network methods have been widely applied to coupling analysis and structural characterisation in various engineering systems. In engineering practice, complex network theory has become a powerful tool for quantifying coupling interactions and topological characteristics of complex mechanical and electromechanical systems. Focusing on mechanical equipment, Peng et al. [40] adopted complex network modelling to analyse module-level coupling relationships of CNC machine tools and identified critical components based on node degree centrality. For general complex electromechanical systems, Xia et al. [41] constructed interdependent network models to reveal system coupling mechanisms and predict failure propagation paths. Targeting railway systems, Lin et al. [42] established network representations to explore coupling and failure propagation paths within high-speed train systems and locate key coupling nodes.

As a fundamental theoretical basis, Ladyman et al. [43] clarified the essential properties of complex systems, highlighting that mutual interaction and multi-dimensional dependency are core features that distinguish complex engineered systems from simple structures. From the perspective of network modelling, Mahabadi et al. [44] reviewed state-of-the-art multilayer network applications for infrastructure systems and demonstrated that practical engineering systems commonly form multilayer coupling structures across mechanical, electrical, and control domains. Cross-layer dependencies allow local faults to propagate through physical, informational, and power coupling paths, resulting in system-level performance degradation [17]. Further, Aleta et al. [45] systematically summarised mainstream topological metrics for multilayer network analysis, confirming that node degree and coupling strength are the most prevalent indicators for evaluating system coupling complexity and robustness.

However, existing studies share three common limitations: (1) edge weights are predominantly assigned based on expert judgement, with a lack of physics-based quantitative methods; (2) network analyses are largely confined to topological characterisation (e.g., degree distribution, clustering coefficient, and community structure), without adequately capturing the higher-order interactive relationships among coupling paths; and (3) there remains a disconnect between network analysis results and decoupling decisions, as a systematic mapping mechanism from network diagnostics to decoupling interventions is absent.

To address these limitations, this paper proposes an undirected weighted graph construction method based on a residual coupling matrix, and establishes a **coupling elasticity matrix** to capture the higher-order interactions among coupling paths. On this basis, a complete decoupling decision chain is developed, spanning from network diagnostics to the assignment of P0–P3 priority labels. Unlike existing complex network analyses that focus primarily on *describing* the coupling network structure, this paper further translates the network analysis results into actionable decoupling recommendations, thereby bridging the gap between network diagnostics and engineering decision-making.

3. Methodology

The methodology is motivated by a theoretical problem: the Independence Axiom of Axiomatic Design (AD) is necessary but not sufficient for system integrability, because it does not constrain physical-field coupling. Theorem 1 formalizes this representational incompleteness and motivates a dual-domain extension of AD.

Theorem 1 challenges this assumption: functional independence does not entail physical independence, and any function-centric mapping M_{F-P} necessarily outputs only functional components C_{func}, while omitting the decoupling components C_{dec} required to suppress physical-field interactions. The central design problem, therefore, is not how to optimize known couplings, but how to co-generate functional and decoupling components during architecture synthesis.

To address this problem, the proposed dual-domain mapping framework treats the functional domain and the physical-field domain as co-equal representational structures. This position is operationalized through four research questions (RQ1–RQ4), as summarized in Table 1. RQ1 addresses the co-generation of functional and decoupling components; RQ2 addresses rapid evaluation of large-scale architectures; RQ3 addresses network diagnosis and decoupling prioritization; and RQ4 addresses verification and validation. Table 1 maps each RQ to a specific metric, measurement, and computational method.

Table 1 Metric–measure–method mapping for the four research questions.

Motivation	Metric	Measure	Method
RQ1: Extension of AD: joint representation and generation of functional and decoupling components	Residual coupling R_{ij}; decoupling component set C_{dec}	Residual coupling matrix (Eq. 20–21); latent coupling inference (Eq. 22–26)	FBS-TRIZ mapping; L0–L1.5 layers
RQ2: Rapid evaluation of large-scale architectures	7 performance indicators; GNN prediction error	CSP enumeration; GNN training/test RMSE	CSP screening (3.2); GNN surrogate (3.4); Pareto optimization (3.5)
RQ3: Network diagnosis and decoupling prioritization	Path degree d_p; stability index Ω; P0–P3 labels	coupling elasticity matrix X; positive feedback detection; priority score W_p	Complex network analysis (3.9–3.11)

RQ4: Theoretical verification and validation	Verification: code/analytical cross-checking, numerical stability, degeneracy testing. Validation: conceptual validation, boundary-condition analysis, external consistency, sensitivity analysis, falsifiable predictions	Degeneracy test pass/fail; sensitivity range; number of falsifiable predictions; external consistency results	Verification and Plausibility Assessment (Section 5)

This mapping ensures that every claim in this paper is traceable to a specific metric, a concrete measurement, and a computational method. It also clarifies why the proposed framework is necessary: existing methods lack metrics for decoupling component generation, measurement procedures for latent coupling, and methods for prioritizing decoupling interventions.

The proposed framework adopts a complex network approach to establish a coupling network model of the system. The essence of coupling lies in the mutual influence between pairs of physical entities, mediated by physical fields such as force, heat, vibration, and electromagnetism. Its fundamental characteristic is symmetry: if component A exerts a physical action on component B, component B necessarily exerts a reaction of some form on component A—this is a basic property of physical systems. Coupling relations are therefore inherently bidirectional, making them well-suited to representation by an undirected weighted graph. In this model, nodes represent functional components and boundary nodes, edges represent coupling relations, and edge weights are given by the residual coupling matrix R, which quantifies the coupling intensity that persists after feasible decoupling measures have been applied.

Compared with data-driven graph neural network approaches, complex network methods offer **distinct advantages** in this study. First, interpretability: the prioritization of coupling paths is grounded in explicit mathematical criteria (residual intensity, path degree, positive feedback loop detection), enabling designers to trace the reasoning chain behind each decision, rather than relying on a black-box model. Second, deep diagnosis of a single network: the object of analysis in this study is the coupling network of a single optimal architecture, and complex network methods can directly perform topological analysis and diagnosis on this network without requiring a large number of training samples. Third, theoretical consistency: metrics such as the residual matrix R, the coupling elasticity matrix X, and the path degree $d_p$are all constructed directly from network topology and numerical analysis, corresponding one-to-one with the coupling mechanisms and thus possessing clear physical meaning.

The specific implementation of the network analysis was carried out using the NetworkX library. Based on the residual coupling matrix Rdefined at layer L1, an undirected weighted graph $G = (V, E, R)$was constructed, where Vdenotes the node set (comprising internal components and boundary nodes) and Edenotes the edge set (node pairs for which $R_{ij} > 0$). This graph structure serves as the unified data substrate for all subsequent analyses—centrality computation, network density evaluation, common-neighbor analysis, path degree calculation, positive feedback loop detection, and network visualization. Building on this foundation, the **coupling elasticity matrix** $X$was computed via numerical differentiation to capture higher-order interactions among paths; the path degree $d_p = \sum_{q \neq p} |X_{pq}|$was obtained by row summation, quantifying the total influence of each path within the elasticity space; and positive feedback loops were identified via the criterion $X_{pq} \cdot X_{qp} > 0$, localizing potentially destabilizing structures. Finally, by integrating residual intensity, path degree, and positive feedback loop risk, a P0–P3 priority label was assigned to each path, yielding a ranked list of decoupling targets.

The L0–L5 layers form a progressive analytical chain: L0 defines the node set and physical-field annotations; L1 quantifies explicit, implicit, and boundary couplings and constructs the residual coupling matrix R; L1.5 infers latent couplings from known network topology and physical-field overlap; L2 builds the **coupling elasticity matrix** X to capture higher-order path interactions; L3 integrates all preceding outputs into a system-level coupling network G=(V,E,R); L4 performs network diagnostics and assigns P0–P3 priority labels; and L5 translates the ranked results into structured decoupling recommendations. Each layer takes the output of the previous layer as its input, forming a continuous chain from coupling representation to decoupling decision support.

The remainder of this section follows this logic. Section 3.1 formalizes the incompleteness of functional-to-physical mapping. Sections 3.2–3.5 present the architecture generation and evaluation pipeline. Sections 3.6–3.12 develop the L0–L5 coupling analysis and decoupling decision layers. Section 3.13 describes the computational implementation. The complete framework is illustrated in Figure 1.

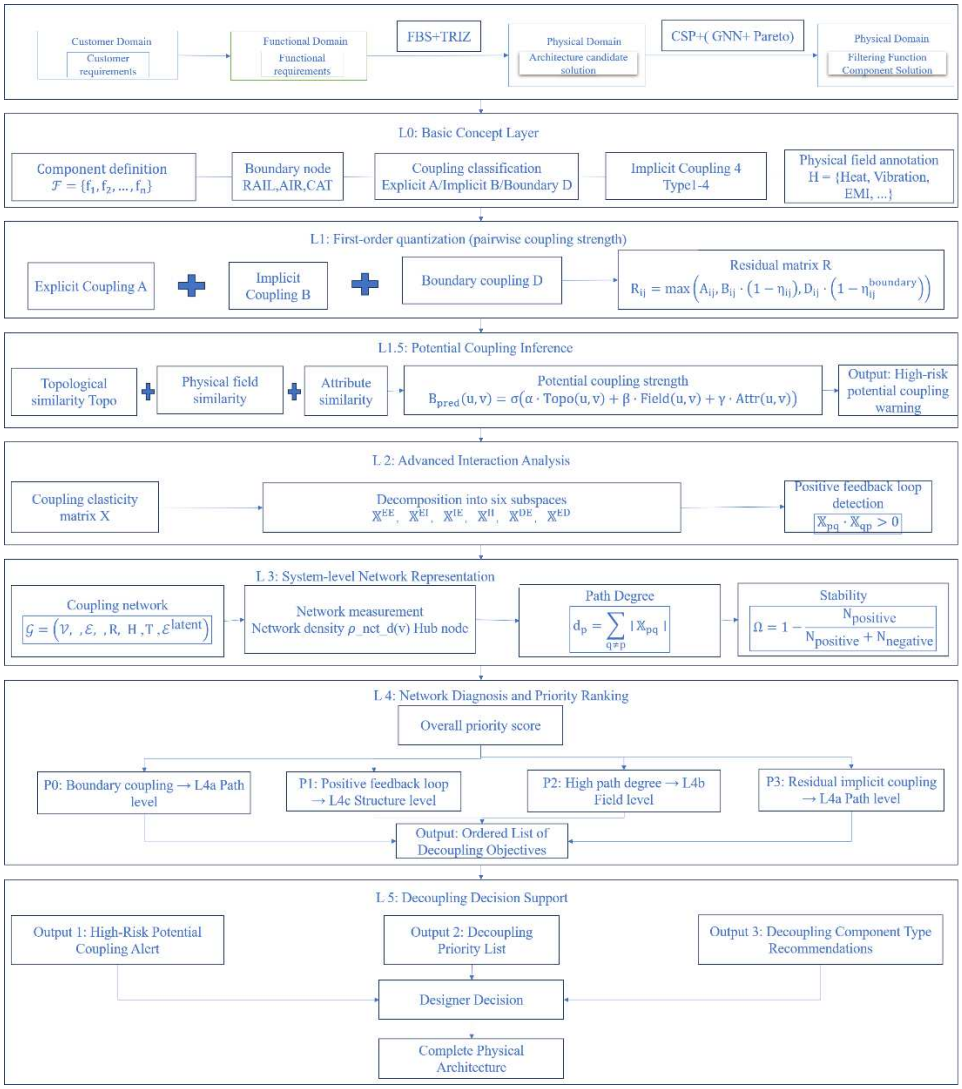


Figure 1 Physical architecture generation framework integrating TRIZ, FBS, and decoupling theory

3.1 Problem Formulation: Incompleteness of Functional–Physical Mapping

The scientific question addressed in this paper is: does functional independence imply physical independence? If not, what representational extension of function-oriented design theory is required to characterize physical-field coupling and generate decoupling components?

Axiomatic Design (AD) assumes that satisfying the Independence Axiom yields a valid architecture. This assumption, however, is incomplete when physical fields are considered. While FBS, TRIZ, and DSM share this limitation, AD provides the most formalized expression of the gap, and therefore the most direct target for extension.

Functionally independent components can still couple through shared physical fields (vibration, electromagnetic interference, heat flow, acoustics, etc.), and some of these couplings cause product performance and quality to fall short of design requirements. To meet those requirements, correct decoupling components must be added—yet decoupling components, which fulfill no functional requirement but serve solely to suppress physical-field coupling, have no representational locus within AD (or, more broadly, within FBS, TRIZ, and DSM). The direct consequence of this representational gap is that existing theories can generate only functional components and cannot guide the generation of decoupling components; the resulting physical architecture is therefore incomplete. Once the system is integrated, problems such as vibration, noise, electromagnetic interference, and thermal failure emerge, making it difficult for product performance and quality to meet requirements, often necessitating repeated revisions or even causing safety incidents. Function-centric design theory alone is thus insufficient to support the generation of a complete physical architecture. What is needed is a representational extension of AD capable of expressing both functional logic and physical-field coupling simultaneously, so as to guide the generation of decoupling components, yield a complete physical architecture, and ensure that product performance and quality meet requirements. Theorem 1 formalizes this incompleteness.

Design problem. The design problem is formulated for the physical architecture synthesis stage of complex electromechanical systems. Given functional requirements, candidate subsystem solutions, physical-field annotations, and known coupling records, how can system architects:

1. identify explicit, implicit, and boundary couplings that functional decomposition cannot represent;
2. infer latent couplings that have not yet been documented;
3. prioritize high-risk coupling paths under limited design resources; and
4. generate or recommend decoupling components alongside functional components, while retaining explicit couplings as hard constraints and satisfying safety, compatibility, cost, and performance constraints?

Metric–measure–method mapping. The following table specifies the design stage, decision-makers, inputs, outputs, objectives, constraints, metrics, measures, methods, validation criteria, and success criteria. **Table 2 summarizes the design problem specification, including decision context, inputs and outputs, objectives, constraints, metrics, methods, and validation/success criteria.**

Table 2. Specification of the design problem: context, decisions, metrics, methods, and validation criteria.

Element	Specification
Design stage	Physical architecture synthesis
Decision-makers	System architects, NVH engineers, subsystem engineers
Decisions	Select subsystem schemes; identify and prioritize couplings; recommend decoupling components
Inputs	Functional requirements; candidate schemes; physical-field annotations; known coupling records
Outputs	Feasible architectures; residual coupling network; P0–P3 decoupling list; recommended decoupling component types
Objectives	Minimize cost, noise, energy, braking distance; maximize stability and decoupling efficiency
Constraints	Safety, compatibility, space, thermal, electromagnetic, cost
Metrics	Residual coupling R_{ij}; path degree d_p; stability index Ω; suppression rates; GNN prediction error; expert agreement
Measures	Residual coupling matrix; latent coupling inference; **coupling elasticity matrix**; positive feedback loops; P0–P3 priority score
Methods	FBS–TRIZ mapping; CSP screening; GNN surrogate; Pareto optimization; complex network analysis; expert knowledge base matching
Validation criteria	Type I: code/analytical cross-checking, numerical stability, enumeration correctness, degeneracy test. Type II: conceptual validation, external consistency with published bench/field data, sensitivity analysis, falsifiable predictions, qualitative comparison with DSM/AD/rule-based/simulation/linear regression
Success criteria	Expert-accepted coupling paths; priority ranking consistent with expert judgment; implementable decoupling recommendations

Scope and boundaries. The framework is demonstrated on a 67-node high-speed train architecture with 2,187 combinations reduced to 468 feasible architectures. All suppression rates are theoretical predictions under assumed decoupling efficiencies, not measured values. Hardware-in-the-loop and prototype testing are outside the scope of this theoretical and methodological study and are identified as future work for engineering implementation.

Relation to existing knowledge. This problem formulation is grounded in the related work reviewed in Section 2. FBS, TRIZ, AD, and DSM provide powerful functional representations but lack a representational slot for physical-field coupling and for components that realize no functional requirement. The proposed dual-domain mapping framework is a direct response to this gap. The formal definitions and the incompleteness theorem are presented in Sections 3.1.1–3.1.3.

In this paper, "co-generation" is defined as the joint representation, evaluation, and decision-making of functional and decoupling components within a single architecture synthesis process. It does not mean that decoupling components are generated from scratch by a computational algorithm. Instead, it means that decoupling components are (i) represented as first-class design objects alongside functional components, (ii) evaluated jointly with functional components under shared objectives and constraints, and (iii) prioritized and recommended within the same decision framework. This definition distinguishes co-generation from conventional post-hoc decoupling, in which decoupling components are introduced only after integration problems have surfaced.

3.1.1 The Functional Domain and the Physical Domain

Definition 1 (Functional Component). Let the target system, through engineering decomposition, yield n functional components, forming a finite set: $F = \{f_1, f_2, \dots, f_n\}$.

where each $f_i$is a unit with well-defined physical boundaries and a distinct function. The decomposition is governed by three criteria: (i) functional autonomy—each component constitutes a self-contained functional unit that cannot be further subdivided; (ii) distinct identity—each component is assigned a unique identifier for traceability; (iii) interface transparency—all inter-component interactions are fully specified through their interfaces.

A functional-to-physical mapping $M_{F\to P}: F \mapsto C_{\text{func}}$is any transformation that converts functional requirements into physical components. FBS, TRIZ, and Axiomatic Design are all instances of such mappings. They share the same output type: a set of functional components C_{func}. None of them produces decoupling components.

Definition 2 (Physical Field). Each functional component $c_i$generates or responds to one or more physical fields in physical space—mechanical vibration, electromagnetic radiation, thermal flux, acoustic pressure, and the like. The set of physical fields associated with $c_i$is denoted $H(c_i)$.

Definition 3 (Field Response Function). For each component $c_i$and each physical field $h \in H(c_i)$, let $G_i^{(h)}: \Omega \times \mathbb{R}_{\geq 0} \to \mathbb{R}$.

denote the field response function of $c_i$in field h, defined over the shared spatial domain $\Omega \subset \mathbb{R}^3$and time $t \geq 0$. The function $G_i^{(h)}(x,t)$represents the intensity of field $h$generated by $c_i$at spatial point $x$and time t.

Definition 4 (Field Interaction Intensity). The field interaction intensity between components $c_i$and $c_j$is defined as

$$\Psi_{ij} = \sum_{h \in H(c_i) \cap H(c_j)} \frac{\left| \left\langle G_i^{(h)}, G_j^{(h)} \right\rangle_{L^2(\Omega \times \mathbb{R}_{\geq 0})} \right|}{\| G_i^{(h)} \|_{L^2} \ \| G_j^{(h)} \|_{L^2}}$$

where the L^2inner product is taken over the shared spatial domain and the operational time horizon. By construction, $\Psi_{ij} \in [0,1]$, with $\Psi_{ij} = 0$indicating no shared-field interaction and $\Psi_{ij} = 1$indicating maximal overlap.

Definition 5 (Field Orthogonality). Two components $c_i$and $c_j$are said to be field-orthogonal if their respective field response functions satisfy $\left\langle G_i^{(h)}, G_j^{(h)} \right\rangle_{L^2(\Omega \times \mathbb{R}_{\geq 0})} = 0$

for every shared physical field $h \in H(c_i) \cap H(c_j)$. Equivalently, $\Psi_{ij} = 0$.

Definition 6 (Physical Independence). Components $c_i$and $c_j$are physically independent if they are field-orthogonal under all admissible boundary conditions and material configurations: $\Psi_{ij}(B,M) = 0 \ \forall (B,M) \in \mathcal{B} \times \mathcal{M}$.

where $\mathcal{B}$denotes the set of admissible boundary conditions and $\mathcal{M}$the set of admissible material configurations. If there exists at least one admissible $(B,M)$for which $\Psi_{ij}(B,M) > 0$, the two components are said to be physically coupled.

Definition 7 (Engineering Threshold). Let $\epsilon > 0$denote an engineering threshold on field interaction intensity, chosen such that $\Psi_{ij} \leq \epsilon$is considered acceptable for the intended operating envelope. The specific value of $\epsilon$is domain-dependent and determined by engineering requirements (e.g., NVH targets, EMC compliance levels, thermal limits).

3.1.2 Representational Incompleteness of Functional-to-Physical Mapping

Theorem 1 (Representational Incompleteness). Let $M_{F \to P}$be a function-centric mapping that generates $C_{\text{func}}$from functional requirements and compatibility constraints. If there exists a pair $(c_i, c_j) \subseteq C_{\text{func}}$such that:

1. $c_i$and $c_j$are functionally independent, i.e., their FR–DP dependency matrix is diagonal or triangular; and
2. the residual coupling strength Ψ_{ij}exceeds a given engineering threshold ϵ, i.e., $\Psi_{ij} > \epsilon$;

then $M_{F \to P}$is representationally incomplete with respect to ϵ: it cannot represent Ψ_{ij}, and it cannot generate the decoupling components C_{dec}required to suppress Ψ_{ij}.

Assumptions. The theorem rests on three assumptions:

1. Functional independence is defined by FR–DP dependency relationships; it does not constrain field orthogonality.
2. Physical fields are defined over spatially extended domains; components that share a spatial region may interact through common physical fields.
3. $M_{F \to P}$outputs only components that realize functional requirements; it has no representational slot for components that realize no functional requirement.

Remark. This theorem is not a claim that AD is wrong; it is a claim that AD's representational scheme requires an additional dimension. Extending AD with a physical-field domain is therefore a structural extension, not a local patch.

Proof. We proceed in four steps.

Step 1: Formal definition of FR–DP independence. Let $\{F, R_1, \ldots FR_n\}$ denote the functional requirements and $\{D, P_1, \ldots DP_n\}$the design parameters. Functional independence is formalized by the design matrix $A = [A_{ij}]$, where $A_{ij} = \frac{\partial FR_i}{\partial DP_j}$.

The Independence Axiom requires $A$to be diagonal or triangular: $A_{ij} = 0$for $i \neq j$(or $i > j$in the triangular case). This condition constrains only the functional mapping from DPs to FRs; it imposes no constraint on the physical realization of the DPs—material properties, geometric configuration, or boundary conditions.

Step 2: Field coupling strength is independent of FR–DP relationships. By Definition 4, $\Psi_{ij}$is determined by the field response functions $G_i^{(h)}$and $G_j^{(h)}$. These functions depend on:

- the material properties of c_i and c_j (e.g., density, elastic modulus, permittivity);
- the geometric configuration (e.g., spatial proximity, interface geometry);
- the boundary conditions (e.g., mounting stiffness, environmental impedance).

None of these quantities appears in the FR–DP matrix A. Therefore, the condition $A_{ij} = 0$ (functional independence) does not imply $\Psi_{ij} = 0$ (field orthogonality). Formally: $A_{ij} = 0 \not\Rightarrow \Psi_{ij} = 0$.

Step 3: Counterexample. To establish that the implication fails even in simple systems, consider a two-degree-of-freedom spring–mass system. Let two masses m_1 and m_2 be mounted on a common rigid base, each controlled by an independent actuator. The functional requirements are:

- FR_1: control the displacement of m_1;
- FR_2: control the displacement of m_2.

Each FR is controlled by its own DP (actuator force), yielding a diagonal design matrix: $A = \begin{pmatrix} \partial FR_1/\partial DP_1 & 0 \\ 0 & \partial FR_2/\partial DP_2 \end{pmatrix}$.

The system satisfies the Independence Axiom. However, because both masses are mounted on the same base, vibrational excitation of m_1 propagates through the base and couples into m_2. The field response functions $G_1^{(h)}$ and $G_2^{(h)}$ (with h = mechanical vibration) overlap in the shared base domain, so $\left\langle G_1^{(h)}, G_2^{(h)} \right\rangle_{L^2} \neq 0 \Rightarrow \Psi_{12} > 0$.

Thus functional independence holds while field coupling is non-zero, establishing that $A_{ij} = 0 \not\Rightarrow \Psi_{ij} = 0$.

Step 4: Representational incompleteness. The mapping $M_{F\to P}$ produces the set $C_{\text{func}} = \{c_1, \ldots, c_n\}$ of functional components. By Assumption 3, $M_{F\to P}$ has no representational slot for components that realize no functional requirement. A decoupling component d that suppresses Ψ_{ij} (e.g., a vibration isolator inserted between the shared base and m_2) realizes no FR; consequently, $d \notin M_{F\to P}(F)$. Since $\Psi_{ij} > \epsilon$ cannot be represented within $M_{F\to P}$, and since the decoupling component required to reduce Ψ_{ij} below ϵ cannot be generated, $M_{F\to P}$ is representationally incomplete with respect to ϵ.

Corollary 1. The output of any function-centric mapping, taken in isolation, is an incomplete physical architecture: it contains functional components but lacks the decoupling components required for physical-field suppression.

Lemma 1. If two components share a spatial region and participate in at least one common physical field, then functional independence does not imply field independence.

Proof. Functional independence is defined by FR–DP dependency relationships (Step 1 of Theorem 1). Field independence requires orthogonal field distributions, and orthogonality depends on material, geometry, and boundary conditions (Step 2 of Theorem 1), none of which are constrained by FRs. Therefore, even when functional independence holds, $\Psi_{ij} > 0$ may still occur.

Remark on engineering relevance. Theorem 1 is not a claim that functional independence always produces physical coupling. It is a claim about representation: function-centric design theories lack the representational dimension required to express physical-field coupling and to generate decoupling components. This is precisely the gap that the dual-domain framework addresses.

3.1.3 Dual-Domain Representation

The theorem above necessitates elevating physical-field interaction to a knowledge dimension coequal with functional logic. The complete physical architecture is expressed as: $PA = C_{func} \cup C_{dec}$

where C_{dec} denotes the set of decoupling components, whose primary purpose is to suppress physical-field interactions. The Functional Domain and the Physical-Field Domain cannot be merged into a single domain—this constitutes the theoretical foundation of the present framework.

A complete physical architecture is defined as one that contains (i) all functional components required to realize the functional requirements, and (ii) all decoupling components required to suppress residual physical-field couplings below their respective thresholds, while retaining explicit couplings as hard constraints.

3.2 Combinatorial Enumeration and CSP Filtering

Role in the Framework. After generating functional component candidates for each subsystem, the complete architecture for a given combination $X \in C$ is assembled as $PA(X) = C_{func}(X)$. CSP filtering then eliminates combinations that violate hard constraints, retaining only those that proceed to GNN-based performance prediction and multi-objective Pareto optimization.

3.2.1 Combinatorial Space Definition

The full combinatorial space is the Cartesian product of subsystem solution sets, as defined in Eq. (1):

$$C = \prod_{m=1}^{M} S_m\,,\quad |\,C\,| = \prod_{m=1}^{M} K_m \tag{1}$$

where each $X \in C$ corresponds to a complete architecture $PA(X)$, and K_m is the number of candidate solutions for subsystem m.

3.2.2 Constraint Definition

Hard constraints H are defined to eliminate infeasible combinations. These constraints fall into three categories:

- **Safety constraints**: derailment coefficient $d \le d_{max}$, braking distance $L_{brake} \le L_{max}$
- **Operational constraints**: critical speed $v \ge v_{min}$, interior noise $n \le n_{max}$, traction efficiency $\eta_{tr} \ge \eta_{tr,min}$
- **Subsystem-internal residual parameters (optional):** braking system residual shock $r_{brake} \le r_{brake,max}$ and network system residual delay $r_{network} \le r_{network,max}$ may also be used as hard constraints when specified in the subsystem candidate solutions (Table 2). In the present case study, these two parameters are not used as hard constraints; the applied constraints are the three performance constraints listed in Section 4.2 plus a safety check on the derailment coefficient.

In addition to performance constraints, physical compatibility rules are applied to exclude combinations that violate engineering feasibility (e.g., incompatibility between specific subsystem options arising from spatial, electrical, or thermal conflicts). These rules are domain-specific and are defined on a per-case basis.

3.2.3 CSP Screening

The feasible region F is obtained by retaining only combinations that satisfy all hard constraints, as defined in Eq. (2):

$$F = \{X, \in C \mid \forall \phi \in H\phi(X) \text{ holds}\} \tag{2}$$

For $|\,C\,|$ on the order of thousands, enumeration-verification is computationally feasible. The resulting feasible architectures F serve as the input to the GNN-based performance prediction (Section 3.4) and subsequent multi-objective Pareto optimization (Section 3.5).

3.3 Performance Aggregation with Nonlinear Coupling Terms

Rationale. Unlike simple linear aggregation, we model nonlinear interactions between performance metrics to capture cross-disciplinary couplings. These nonlinearities — captured as cross-terms — provide the formal justification for using a GNN surrogate instead of linear regression. Each feasible architecture is mapped to a 7-dimensional performance vector, as expressed in Eq. (3):

$$f(X) = \big(C(X), N(X), E(X), B(X), D(X), -U(X), -L(X)\big) \tag{3}$$

where each component is defined below.

3.3.1 Linear Components

The following indicators are directly determined by subsystem selections:

Total cost is the linear accumulation of manufacturing costs across all subsystems, as given in Eq. (4):

$$C(X) = \sum_{m=1}^{M} C_{m,i_m} \tag{4}$$

In-cabin noise is directly determined by the selection of the car body subsystem, as expressed in Eq. (5):

$$N(X) = n_{\text{carbody},i_{\text{carbody}}} \tag{5}$$

Derailment coefficient is directly determined by the selection of the bogie subsystem, as given in Eq. (6):

$$D(X) = d_{\text{bogie},i_{\text{bogie}}} \tag{6}$$

Comfort level is directly determined by the selection of the passenger service subsystem, as defined in Eq. (7):

$$U(X) = u_{\text{service},i_{\text{service}}} \tag{7}$$

Auxiliary power supply lifespan is directly determined by the selection of the auxiliary power subsystem, as shown in Eq. (8):

$$L(X) = l_{\text{aux},i_{\text{aux}}} \tag{8}$$

3.3.2 Nonlinear Components (Coupling Cross-Terms)

Energy Consumption with Coupling Amplification: Energy consumption per 100 km per capita is calculated by considering baseline consumption and traction efficiency losses, with an additional nonlinear coupling cross-term, as formulated in Eq. (9):

$$E(X) = E_0 + \sum_{m} e_{m,i_m} + \lambda_{NE} \cdot d_{\text{brake}}(X) \cdot N(X) \tag{9}$$

where $d_{\text{brake}}(X)$ is the delay time parameter of the braking subsystem. The term $\lambda_{NE} \cdot d_{\text{brake}}(X) \cdot N(X)$ captures the nonlinear amplification effect: higher braking-system delay amplifies the energy consumption of noise suppression systems.

Braking Distance with Coupling Interaction: Emergency braking distance is determined by the delay time of the braking subsystem, with an additional nonlinear interaction term, as given in Eq. (10):

$$B(X) = B_0 + \lambda_B \cdot d_{\text{brake}} + \lambda_{DB} \cdot d_{\text{brake}} \cdot N(X) \tag{10}$$

where $\lambda_{NE}, \lambda_B,$ and λ_{DB} are empirically determined influence coefficients, and d_{brake} is the known delay time parameter of the braking subsystem.

3.4 GNN Surrogate for Rapid Performance Prediction

The GNN is used here as a surrogate model for rapid performance prediction. It is not the theoretical core of the framework. The core contributions are the residual coupling matrix R(L1), the **coupling elasticity matrix.**

coupling elasticity matrix X(L2), path degree $d_p$and positive feedback loop detection (L3–L4), and P0–P3 priority ranking (L4). The GNN can be replaced by other surrogate models or high-fidelity simulation without altering the theoretical foundation.

Why a Surrogate is Necessary. Evaluating all feasible architectures using high-fidelity simulation would require hours per architecture — computationally prohibitive for the **468 candidates** obtained from CSP screening. A surrogate model that predicts performance in seconds enables practical design-space exploration and rapid iteration.

Why GNN (Not Linear Regression). Due to the nonlinear cross-terms in Section 3.3 (e.g., $d_{\text{brake}} \cdot N$), the mapping $X \mapsto f(X)$ is intrinsically nonlinear. Graph Neural Networks, as universal function approximators on graph-structured data, are well-suited to learn this nonlinear mapping from subsystem configuration graphs to performance vectors.

Graph Representation. Each architecture $X \in F$ is represented as a graph $G_X = \{V, E\}$:

- **Nodes** $V = \{1, .., .. M\}$: subsystems with node features including cost, efficiency, and other subsystem-level parameters.
- **Edges** E: coupling relationships between subsystems. Edge weights $w_{ij} = y_{ij}$ quantify the design dependency intensity.

Graph Convolutional Network Architecture. The GNN employs a two-layer Graph Convolutional Network (GCN) followed by global average pooling and fully connected layers. The convolution operation at layer l is formally defined by Eq. (11):

$$h_m^{l+1} = \sigma\left(\sum_{n \in N(m)} \frac{1}{\sqrt{\deg(m)\deg(n)}} W^l h_n^l \right) \tag{11}$$

where h_m^l is the feature vector of node m at layer l, $N(m)$ is the neighbor set, $\deg(m)$ is the degree of node m, W^l is the learnable weight matrix, and σ is the activation function.

After the convolutional layers, global average pooling aggregates node-level representations into a single graph-level vector: $h_{\text{graph}} = \frac{1}{M} \sum_{m=1}^{M} h_m^L$. This graph-level representation is then passed through fully connected layers to output the prediction vector $\hat{y}(X)$.

Outputs. The GNN predicts a 7-dimensional performance vector: $\hat{y}(X) = \left(\hat{C}, \hat{N}, \hat{E}, \hat{B}, \hat{D}, -, \hat{U} - \hat{L}\right)$.

Training. The model is trained using Mean Squared Error (MSE) as the loss function, as expressed in Eq. (12):

$$L = \frac{1}{| F |} \sum_{X \in F} \| \hat{y}(X) - y(X) \|_2^2 \tag{12}$$

The Adam optimizer is employed for parameter updates. The dataset of 468 feasible architectures is randomly split into training and test sets with an 80%/20% ratio. Training proceeds for 500 epochs with early stopping.

The GNN serves as a surrogate for rapid design-space exploration when the candidate space grows beyond the 468 architectures considered here. For the present case study, the 468 architectures are small enough that exhaustive enumeration is computationally feasible; the GNN is therefore presented as a scalable option for larger design spaces, not as a necessity for the present case.

3.5 Multi-Objective Pareto Optimization Screening

Based on the performance vector $f(X)$ defined in Section 3.3, we perform multi-objective optimization to identify Pareto-optimal architectures from the feasible set F (filtered in Section 3.2).

3.5.1 Multi-Objective Problem Statement

The multi-objective optimization problem is formulated as the simultaneous minimization of the 7 performance indicators. This is a multi-objective optimization problem: no single architecture can simultaneously minimize all objectives; trade-offs are inevitable.

3.5.2 Pareto Dominance Relation

For two schemes $X_1, X_2 \in F$, X_1 is said to dominate X_2 if and only if the condition in Eq. (13) is satisfied:

$$\forall j, f_j(X_1) \leq f_j(X_2) \text{ and } \exists j, f_j(X_1) < f_j(X_2) \tag{13}$$

The Pareto optimal set is the collection of all non-dominated solutions, as formally defined in Eq. (14):

$$P = \{X, \in F \mid \nexists X' \in FX' \text{ dominates } X\} \tag{14}$$

3.5.3 Fast Non-Dominated Sorting Algorithm

To obtain the Pareto frontier, we employ the fast non-dominated sorting algorithm from NSGA-II [36]. The algorithm hierarchically partitions F into fronts $F_1, F_2, \ldots$, where $F_1 = P$ (the Pareto frontier).

3.5.4 Comprehensive Recommendation (Weighted Sum Method)

We employ the weighted sum method with normalized objective values. The objective values are first normalized, as expressed in Eq. (15):

$$\tilde{f}_j(X) = \frac{f_j(X) - f_j^{\min}}{f_j^{\max} - f_j^{\min}} \tag{15}$$

A weight vector $w = (w_1, w_2, .., .. w_7)$ is introduced with $\sum_{j=1}^{7} w_j = 1$. **The comprehensive score for each architecture is then computed as follows, as shown in Eq. (16):**

$$\text{Score}(X) = \sum_{j=1}^{7} w_j \cdot \tilde{f}_j(X) \tag{16}$$

The scheme with the minimum score is recommended as the comprehensive optimal architecture, as expressed in Eq. (17):

$$X^* = \arg\min_{X \in P} \text{Score}(X) \tag{17}$$

Remark. In practice, we restrict the weighted sum selection to the Pareto frontier P, ensuring that the recommended architecture is Pareto-optimal.

3.6 L0: Foundational Concept Layer — Nodes, Coupling, and Physical Fields

L0 constitutes the foundational layer of the entire analytical framework, responsible for abstracting the physical system into a node set within graph theory and assigning physical-field attributes to each node.

3.6.1 Complete Node Set

Definition 8 (Boundary Node): A boundary node $v \in V_{boundary}$is an external entity situated at the boundary of the system. Typical boundary nodes include mechanical boundaries (track, foundation), fluid boundaries (air, water), and energy boundaries (power grid, catenary).

Definition 9 (Complete Node Set): The complete node set of the system is the union of internal functional components and boundary nodes: $V = V_{internal} \cup V_{boundary}$

where $\mid V_{internal} \mid = n$and $\mid V_{boundary} \mid = b$.

Boundary nodes simultaneously function as both sources of coupling (e.g., track irregularities exciting vibration) and sinks of coupling (e.g., vibration energy dissipated to the track), and must therefore be treated as first-class citizens throughout all subsequent analyses.

3.6.2 Coupling Classification

Definition 10 (Coupling): Coupling refers to the mutual influence arising between two or more functional components, or between a component and a boundary node, as a result of physical connection or a shared physical field.

- **Explicit Coupling A_{ij}:** Coupling that is deliberately introduced at the design stage and formally recorded in interface documentation—for example, bolted joints, wiring harnesses, and signal communication links.
- **Implicit Coupling B_{ij}:** Coupling that escapes detection during the design stage and becomes apparent only when components are integrated or when the system operates under certain conditions—for instance, through shared physical fields or contention for common resources.
- **Boundary Coupling D_{ij}:** Coupling between internal components and boundary nodes (e.g., wheel-rail interaction, pantograph-catenary contact).

Generalized Coupling: $C_{ij} = A_{ij} + B_{ij} + D_{ij}$.

3.6.3 Four-Category Classification of Implicit Coupling

Building upon the classification framework established in prior work [39], this study categorizes implicit coupling into four types according to their physical decouplability and response characteristics: *cuttable-type* (eliminable through physical isolation measures), *contractual-constraint-type* (constrainable through interface timing contracts), *coordination-dependent-type* (suppressible through active runtime coordination), and *adaptive-architecture-type* (accommodable through dynamic module

reconfiguration in response to environmental changes). The preset decoupling efficiencies η for these four categories are set at 0.98–1.00, 0.80–0.95, 0.85–0.95, and 0.90–0.98, respectively, serving as prior parameters for residual matrix computation at the L1 layer.

Consistent with the η-value framework established in [39], specific decoupling efficiencies are further assigned to individual coupling paths based on engineering practice and physical principles. For instance, optical fiber isolation achieves near-complete electromagnetic decoupling ($\eta = 1.00$); independent busbar architectures provide effective electrical isolation ($\eta = 0.99$); thermal coordinators offer moderate suppression of thermal–mechanical coupling ($\eta = 0.90$); and active vibration isolators yield high vibration suppression ($\eta = 0.95$). These values represent theoretical priors derived from established technological capabilities and can be readily replaced with experimentally validated or simulation-verified efficiencies for specific design contexts, without compromising the validity of the proposed framework. A sensitivity analysis of η is provided in Section 5.3.

3.6.4 Physical Field Annotation

Each component and each coupling path is associated with one or more physical fields. The complete set of physical fields is as shown in Equation (18):

$$H = \{H_{\text{thermal}}, H_{\text{vibration}}, H_{\text{EMI}}, H_{\text{acoustic}}, H_{\text{fluid}}, H_{\text{mechanical}}, H_{\text{temporal}}\} \tag{18}$$

Let $H(f_i) \subseteq \mathcal{H}$ denote the set of physical fields in which component f_i participates, and let $H(p) \subseteq \mathcal{H}$ denote the physical field label of coupling path p.

3.7 L1: First-Order Quantification—Pairwise Coupling Intensity and Residual Matrix

The L1 layer is responsible for quantifying the identified coupling relationships in the system and computing the residual coupling matrix.

3.7.1 Explicit Coupling Matrix A

Definition 11 (Explicit Coupling Matrix): $A = [A_{ij}]_{(n\times n)}$ is a real symmetric non-negative matrix, with $A_{ij} \in [0,1]$, $A_{ij} = A_{ji}$, and $A_{ii} = 0$, as shown in Equation (19).

$$A_{ij} = \max\left(A_{ij}^{\text{base}}, A_{ij}^{\text{interface}}\right) \tag{19}$$

where A_{ij}^{base} is determined based on subsystem affiliation (0.3 for components within the same subsystem, and 0.05 otherwise), and $A_{ij}^{\text{interface}}$ is determined by the strongest physical interface (0.8 for a direct mechanical connection, 0.7 for an electrical connection, 0.5 for a signal connection, 0.4 for energy transmission, 0.2 for indirect environmental interaction, and 0.05 for no direct interface).

where A_{ij}^{base} takes the value 0.3 if the two components belong to the same subsystem, and 0.05 otherwise; $A_{ij}^{\text{interface}}$ is determined by the strongest physical interface: 0.8 for a direct mechanical connection, 0.7 for an electrical connection, 0.5 for a signal connection, 0.4 for energy transmission, 0.2 for indirect environmental interaction, and 0.05 when no direct interface exists.

3.7.2 Implicit Coupling Matrix B

Definition 12 (Implicit Coupling Record): Each implicit coupling instance is represented as a six-tuple $c = (i, j, s_c, \tau_c, \eta_c, d_c)$, where s_c denotes the raw coupling intensity, $\tau_c \in \{1,2,3,4\}$ indicates the coupling type, η_c is the decoupling efficiency, and d_c identifies the decoupling target.

Definition 13 (Implicit Coupling Matrix): $B = [B_{ij}]_{n\times n}$ is a real symmetric non-negative matrix, with $B_{ij} = \max_{c\in\mathcal{C}_{ij}} s_c$, where $\mathcal{C}_{ij}$ denotes the set of implicit coupling instances between components i and j.

3.7.3 Boundary Coupling Matrix D

Definition 14 (Boundary Coupling Matrix): $D = [D_{ij}]_{n\times n}$ is a real symmetric non-negative matrix, where D_{ij} is determined according to the boundary node type (RAIL/AIR/CAT). Each boundary coupling is associated with a decoupling efficiency $\eta_{ij}^{\text{boundary}}$.

3.7.4 Residual Coupling Matrix R

The residual coupling matrix R introduced in this section is the operational instantiation of the field interaction intensity Ψ_{ij} defined in Definition 4. Specifically, R_{ij} is computed by applying engineering decoupling efficiencies η to Ψ_{ij}.

The residual coupling matrix R is the operational instantiation of Ψ_{ij}: R_{ij} is computed by applying engineering decoupling efficiencies η to Ψ_{ij}.

Explicit-Coupling-Priority Principle: Explicit coupling A constitutes a hard constraint—the physical prerequisite for the realization of system functionality. Implicit coupling B and boundary coupling D constitute soft constraints—perturbations that can be attenuated.

Definition 15 (Residual Coupling Matrix): $R = [R_{ij}]_{|V|\times|V|}$ is defined as shown in Equation (20):

$$R_{ij} = max(A_{ij},\ B_{ij}(1-\eta_{ij}),\ D_{ij}(1-\eta_{ij}^{boundary})) \tag{20}$$

The residual matrix R is assembled by retaining explicit couplings at their full strength, then aggregating the residual contributions from implicit and boundary couplings. For each implicit coupling record $c = (i, j, s_c, \tau_c, \eta_c, d_c)$, the residual contribution is $r_c = s_c \cdot (1 - \eta_c)$, and the corresponding matrix element is updated as shown in Equation (21), with the max operation preserving the strongest coupling when multiple contributions affect the same component pair.

$$R_{ij} = \max\left(R_{ij}^{\text{existing}}, r_c\right) \tag{21}$$

Physical interpretation: R_{ij} represents the coupling strength that remains after all feasible decoupling measures have been applied.

3.8 L1.5: Latent Coupling Inference — Predicting the Unknown

3.8.1 The Fundamental Problem: Incomplete Design Knowledge

A long-standing yet rarely confronted issue in engineering design practice is that coupling records documented in design specifications are inevitably incomplete. Traditional modular design methods—such as DSM, FBS, and AD—all rest on an implicit assumption: that all relevant interactions have been fully identified and recorded during the design phase. In complex electromechanical systems, however, the invisibility of physical fields and the concealed nature of multi-step propagation paths render a substantial number of implicit couplings fundamentally unidentifiable at the design stage. A complete coupling network model must not only quantify known couplings but also possess the capability to infer unknown ones from known information. This is precisely the core mission of the L1.5 layer.

3.8.2 Two Foundational Assumptions

Assumption 1 (Structural Equivalence): If two components exhibit similar neighborhood structures within the coupling network, they tend to experience similar physical environments and may consequently share undocumented coupling paths.

Assumption 2 (Physical Field Consistency): Physical fields are continuous and propagative in nature. If two components participate in the same physical field, they inevitably interact through that field—regardless of whether this interaction has been recorded in the design documentation.

These two assumptions are mutually complementary: topological structure reveals "who is likely to be structurally related," whereas physical field labels reveal "who must interact physically."

3.8.3 Mathematical Formulation

Definition 16 (Latent Coupling Intensity): For any pair of components (u, v) without a recorded direct coupling, the latent coupling intensity is given by the weighted composition of three independent similarity components, as shown in Equation (22).

$$B_{\text{pred}}(u, v) = \sigma\left(\alpha \cdot \text{Topo}(u, v) + \beta \cdot \text{Field}(u, v) + \gamma \cdot \text{Attr}(u, v)\right) \tag{22}$$

where $\sigma(x) = 1/\left(1 + e^{-10(x-0.2)}\right)$ is the sigmoid function, and $\alpha + \beta + \gamma = 1$.

(1) Topological Similarity

Based on the Resource Allocation (RA) index in network science, as shown in Equation (23).

$$\text{Topo}(u, v) = \sum_{k \in \Gamma(u) \cap \Gamma(v)} \frac{1}{|\ \Gamma(k)\ |} \tag{23}$$

Physical meaning: If two components share a certain neighbor k, and the degree of this neighbor is small (i.e., it is a dedicated connection), then the coupling probability is higher.

(2) Physical Field Similarity (Field Similarity)

The physical field similarity, as shown in Equation (24).

$$\text{Field}_{ij} = \frac{|\ H(f_i) \cap H(f_j)\ |}{|\ H(f_i) \cup H(f_j)\ |} \tag{24}$$

Physical meaning: This indicator measures the extent to which two components share a physical field.

(3) Attribute Similarity

The attribute similarity measures whether two components belong to the same subsystem. It is formally defined as shown in Eq. (25).

$$\text{Attr}(u, v) = \begin{cases} 1, & \text{if } u \text{ and } v \text{ belong to the same subsystem} \\ 0, & \text{otherwise} \end{cases} \tag{25}$$

Physical meaning: Components belonging to the same subsystem typically share similar physical environments, installation conditions, and operating scenarios, and therefore have a higher probability of latent coupling. This formulation converts the engineering heuristic of "whether they belong to the same subsystem" into a binary logical judgment, providing a direct categorical basis for synthesizing latent coupling strength.

The weighting coefficients α, β, γ are set to **0.6, 0.3, and 0.1**, respectively. These weights are configurable engineering priors, not fixed constants. Their default values reflect the relative importance assigned to topological, physical-field, and attribute similarity in latent-coupling inference. Designers may adjust them to reflect different engineering priorities. The framework remains structurally valid under any non-negative weights satisfying $\alpha + \beta + \gamma = 1$. A sensitivity analysis of these weights is provided in Section 5.3.

3.8.4 Inference Procedure

The inference procedure of L1.5 is executed in the following steps:

Step 1: Construct an undirected weighted graph G based on the residual coupling matrix R derived from L1, using a threshold of $\theta = 0.05$.

Step 2: Traverse all component pairs $\{i, j\}$ that are not connected by known edges.

Step 3: For each unconnected pair, compute the topological similarity Topo_{ij}, the physical field similarity Field_{ij}, and the attribute similarity Attr_{ij}.

Step 4: Substitute these three similarity values into the formula to calculate the predicted latent coupling strength B_{ij}^{pred}.

Step 5: Retain paths with B_{ij}^{pred} exceeding the threshold θ_{latent} (typically set to 0.15) and output them as "high-risk latent coupling warnings."

The threshold θ_{latent} is a sensitivity-control parameter, not a fixed constant. Raising the threshold reduces false positives, while lowering it increases coverage of potential coupling paths. Its default value (0.15) is chosen to balance precision and recall in the high-speed train case. A sensitivity analysis of θ_{latent} is provided in Section 5.3.

3.8.5 Extended Implicit Coupling Matrix

The predicted latent coupling strengths are merged with the known implicit couplings to form an extended matrix, as shown in Eq. (26):

$$B_{ij}^{+} = \max\{B_{ij}, B_{ij}^{\mathrm{pred}}\} \tag{26}$$

Important Positioning: $B^{+}$is not intended to supersede documented known records, but rather to augment them. In cases where the inferred results conflict with engineering experience, the documented known records shall take precedence. The role of L1.5 is that of a decision-support tool, not an automated judgment system.

3.8.6 Physical Interpretation and Practical Value

The core value of L1.5 lies in **converting designers' tacit experience into a computable and traceable quantitative indicator**. Its significance does not reside in providing deterministic conclusions, but rather in offering actionable early warnings—shifting the starting point of decoupling efforts from “post-hoc remediation” to “ex-ante warning.”

3.8.7 Degeneracy: L1.5 Reduces to L1

When no shared neighbors exist within the network and the physical-field overlap degree is zero, the potential coupling intensity $B_{ij}^{pred}$is identically zero. In this case, the augmented matrix degenerates to $B^{+} = B$, and the framework seamlessly reverts to the conventional known-coupling model. This degeneracy property ensures that L1.5 constitutes a strict extension of L1, rather than a substitute for or a contradiction to it.

3.9 L2: Second-Order Interactions—The Coupling of Couplings

3.9.1 Definition of Coupling Path

Definition 17 (Coupling Path): A coupling path p is a complete description of the coupling relationship between two nodes $\{i, j\}$, as shown in Equation (27).

$$p = \{i, j, \rho_p, \tau_p, H_p\} \tag{27}$$

where $\rho_p = R_{ij}$ is the residual coupling strength, τ_p denotes the coupling type, and H_p is the physical field label. The complete set of paths is denoted as $P = \{p_1, p_2, \dots, p_m\}$.

3.9.2 **L2: Interaction Analysis Layer — Coupling Elasticity Matrix**

Definition 18 (Coupling Elasticity). For two coupling paths $p = (i, j)$and $q = (k, l)$, the *coupling elasticity* $X_{pq}$is defined as the logarithmic derivative of the generalized coupling strength $C_p$with respect to C_q:

$$X_{pq} = \frac{\partial \ln C_p}{\partial \ln C_q} = \frac{\partial C_p}{\partial C_q} \cdot \frac{C_q}{C_p} \qquad (28)$$

where $C_{ij} = A_{ij} + B_{ij}^{ext} + D_{ij}^{ext}$ is the generalized coupling strength of path p.

Physical interpretation. X_{pq} quantifies the percentage change in the coupling strength of path p corresponding to a 1% variation in the coupling strength of path q. This is the standard definition of *elasticity* in economics and sensitivity analysis, not a tensor in the differential-geometric sense. Specifically:

$X_{pq} > 0$ indicates that path q amplifies path p;

$X_{pq} < 0$ indicates that path q attenuates path p;

$X_{pq} = 0$ indicates that path q has no first-order effect on path p.

The coupling elasticity matrix $X = [X_{pq}]_{m\times m}$ collects the pairwise elasticities of all m coupling paths.

Remark on terminology. The term "matrix" rather than "tensor" is used deliberately: X_{pq} is a Jacobian-based sensitivity coefficient, not a multilinear object that transforms covariantly under coordinate changes. The distinction is important for mathematical precision.

3.9.3 Block Decomposition of the Elasticity Matrix

Since the generalized coupling strength decomposes as $C_{ij} = A_{ij} + B_{ij}^{ext} + D_{ij}^{ext}$, the elasticity matrix X naturally admits a block decomposition into six submatrices according to the coupling category of the source path p and the target path q.

Table 3. Block decomposition of the coupling elasticity matrix.

Block	Expression	Physical meaning	Engineering example
$\boldsymbol{X^{EE}}$	$\partial A_{ij}/\partial A_{kl} \cdot (A_{kl}/A_{ij})$	Explicit-to-explicit elasticity	Bolt load redistribution
$\boldsymbol{X^{EI}}$	$\partial A_{ij}/\partial B_{kl} \cdot (B_{kl}/A_{ij})$	Explicit-to-implicit elasticity	Preload altering contact thermal resistance
$\boldsymbol{X^{IE}}$	$\partial B_{ij}/\partial A_{kl} \cdot (A_{kl}/B_{ij})$	Implicit-to-explicit elasticity	Thermal expansion causing bolt loosening
$\boldsymbol{X^{II}}$	$\partial B_{ij}/\partial B_{kl} \cdot (B_{kl}/B_{ij})$	Implicit-to-implicit elasticity	Thermo-vibration coupling
$\boldsymbol{X^{DE}}$	$\partial D_{ij}/\partial A_{kl} \cdot (A_{kl}/D_{ij})$	Boundary-to-explicit elasticity	Track excitation altering suspension force
$\boldsymbol{X^{ED}}$	$\partial A_{ij}/\partial D_{kl} \cdot (D_{kl}/A_{ij})$	Explicit-to-boundary elasticity	Active suspension modifying wheel–rail contact

Interpretation of the six blocks. The block decomposition clarifies how different coupling categories interact:

- X^{EE} captures the elastic interaction among explicit couplings—these are hard constraints and are typically not decoupled, but their mutual sensitivities reveal load-redistribution effects.
- X^{EI} and X^{IE} capture cross-category interactions between explicit and implicit couplings—these are the pathways through which a functional interface can inadvertently excite an implicit coupling, or vice versa.
- X^{II} captures the interaction among implicit couplings themselves—this is the primary target of decoupling intervention, as it reveals self-reinforcing or mutually attenuating patterns.
- X^{DE} and X^{ED} capture the interaction between boundary couplings and explicit couplings—these are critical for understanding how external disturbances propagate into the functional architecture.

Remark on the block structure. The six blocks are not a "tensor decomposition" in the multilinear-algebraic sense; they are a *categorical partition* of the elasticity matrix according to coupling type. This partition is meaningful because it aligns with the three coupling categories (explicit, implicit, boundary) that underpin the L1 layer.

3.9.4 Positive Feedback Loop Detection

Definition 19 (Positive Feedback Loop): Two paths p and q constitute a positive feedback loop if the condition $X_{pq} \cdot X_{qp} > 0$ is satisfied, indicating that path p amplifies path q, while path q likewise amplifies path p, thereby forming a self-reinforcing cycle. Positive feedback loops are a primary cause of system instability and must be identified and interrupted. Negative feedback loops, characterized by $X_{pq} \cdot X_{qp} < 0$, are self-correcting and contribute to system stability.

3.9.5 **Numerical Computation of the Elasticity Matrix**

In practice, X_{pq} is computed via numerical differentiation on the generalized coupling strength matrix $C = [C_{ij}]$:

$$X_{pq} \approx \frac{C_p(C_q + \Delta) - C_p(C_q)}{\Delta} \cdot \frac{C_q}{C_p} \qquad (29)$$

where $\Delta = \delta \cdot C_q$ is a small perturbation (typically $\delta = 0.01$), and $C_p(C_q + \Delta)$ denotes the value of C_p after perturbing C_q by Δ. The perturbation is applied symmetrically to preserve the undirected nature of the coupling network.

Numerical stability. The step size $\delta = 0.01$ was selected based on a sensitivity analysis (Section 5.3): varying δ from 0.001 to 0.05 produces elasticity entries that remain stable to within 2% relative deviation, with no rank reversals in the

resulting priority ordering.

3.10 L3: System-Level Network Representation—Coupling Network

3.10.1 Definition of Coupling Network

Definition 20 (Coupling Network): The complete coupling state of the system is represented as a weighted, labelled undirected graph, as shown in Equation (30).

$$G = \{V, E, R, H, T, E^{\text{latent}}\} \tag{30}$$

where $V = V_{internal} \cup V_{boundary}$denotes the node set, $E = \{(i,j) \mid R_{ij} > 0\}$denotes the set of known edges, E^{latent}denotes the set of inferred latent edges, $R$is the weight matrix, $H$is the physical field label matrix, and $T$is the coupling type matrix.

3.10.2 Network Topological Metrics

Network Density: as shown in Equation (31).

$$\rho_{\text{net}} = \frac{2 \mid E \mid}{\mid V \mid (\mid V \mid -1)} \tag{31}$$

Node degree: as shown in Equation (32).

$$d(v) = \sum_{j} 1_{(v,j)\in E} \tag{32}$$

Hub Node Identification: Nodes whose degree exceeds the mean by more than twice the standard deviation are identified as hub nodes, as shown in Equation (33).

$$\text{Hub}(v) = \text{True} \iff d(v) > \bar{d} + 2\sigma_d \tag{33}$$

3.10.3 Path Degree

The path degree $d_p$quantifies the global influence of path $p$within the *elasticity space* spanned by all coupling paths:

$$d_p = \sum_{q \neq p} \mid X_{pq} \mid \tag{34}$$

A path degree $d_p > 1.0$indicates that the corresponding path exhibits strong elastic interactions with multiple other paths and thus warrants particular attention in decoupling decision-making. The threshold $d_p > 1.0$is an engineering prior, not a fixed constant; it may be adjusted according to project-specific sensitivity requirements.

3.10.4 Network Stability Index

Definition 21 (Network Stability Index Ω): System stability is quantified as shown in Equation (35).

$$\Omega = 1 - \frac{N_{\text{positive}}}{N_{\text{positive}} + N_{\text{negative}}} \tag{35}$$

where $N_{positive}$and $N_{negative}$denote the number of positive feedback loops and negative feedback loops, respectively. $\Omega > 0$indicates that the system is stable (dominated by negative feedback), while $\Omega < 0$indicates that the system is unstable (dominated by positive feedback). When $N_{positive} + N_{negative} = 0$, $\Omega$is defined as 1.000 by convention.

3.11 L4: Network Diagnostics and Decoupling Prioritization — From Network Analysis to Actionable Decisions

Based on the coupling elasticity matrix $\boldsymbol{X}$defined in Section 3.9, the L4 layer performs network vulnerability diagnostics and priority ranking.

3.11.1 Network Vulnerability Diagnostics

Three diagnostic indicators are employed to identify critical paths:

① Path Vulnerability Index: as shown in Equation (36).

$$V_p = \alpha \cdot \rho_p + \beta \cdot d_p + \gamma \cdot r_p \tag{36}$$

where α, β, γ are weighting coefficients ($\alpha + \beta + \gamma = 1$), $\rho_p$denotes the residual intensity, $d_p$denotes the path degree, and $r_p$denotes the engineering risk level. The weights α, β, γ in Eq. (36) are likewise configurable engineering priors. They are distinct from the similarity weights in Section 3.8.3 and can be adjusted without affecting the framework structure.

② **Positive feedback loop risk**: This is formulated as shown in Equation (37).

$$R(L_k) = \sum_{q=1}^{t} \rho_{p_q} \prod_{q=1}^{t} \mid X_{p_q, p_{q+1}} \mid \tag{37}$$

Let $L_k = \{p_1 \to p_2 \to \cdots \to p_t \to p_1\}$ with $p_{t+1} = p_1$.

③ The cascading risk is then given by Equation (38).

$$C_p = \sum_{q \neq p} \frac{|X_{pq}| \cdot \rho_q}{1 + \mathrm{dist}(p, q)} \tag{38}$$

where $\mathrm{dist}(p, q)$denotes the network distance between paths $p$and q.

3.11.2 Decoupling priority

Based on the comprehensive priority scores, all coupled paths are sorted in descending order of priority $P_0 \rightarrow P_1 \rightarrow P_2 \rightarrow P_3$, as given in Eq. (39).

$$Decoupling\ sequence = \mathrm{sort}\big(P, \text{by } W_p \text{ descending}\big) \tag{39}$$

Overall priority score: As shown in formula (40).

$$W_p = w_1 \cdot V_p + w_2 \cdot \max_{k:p \in L_k} R(L_k) + w_3 \cdot C_p \tag{40}$$

where $w_1 + w_2 + w_3 = 1$. The weights w1, w2, and w3 are engineering priors, not fixed constants. They are configurable by designers according to project-specific priorities. Changing these weights affects the numerical ranking of paths but does not alter the theoretical structure of the L4 priority assignment or the P0–P3 classification rules. A sensitivity analysis is provided in Section 5.3.

Table 4 establishes a priority-based decision mechanism for selecting appropriate decoupling strategies. The priority levels (P0 to P3) reflect the urgency and severity of coupling issues, guiding designers to address the most critical nodes first. **Priority P0** is assigned to nodes involving boundary interfaces (RAIL/AIR/CAT), as these external coupling points directly affect system safety and operational reliability; such nodes require immediate path-level decoupling measures including physical isolation and active control. **Priority P1** applies to nodes participating in positive feedback loops, where coupled interactions are self-reinforcing and may lead to system instability; these cases demand structure-level interventions such as layout reconfiguration or architectural changes to fundamentally break the reinforcing cycle. **Priority P2** covers nodes with high path degree ($d_p > 1.0$), indicating extensive coupling propagation across the system; these nodes call for field-level strategies such as unified thermal management or global EMI shielding to address the shared physical field effects. **Priority P3** includes nodes with high residual strength ($\rho_p > 0.15$) but lower propagation impact, where path-level measures including interface contract specification and software coordination are sufficient. This priority hierarchy ensures that limited design resources are allocated to the most consequential coupling issues first, while lower-priority nodes are addressed with proportionally simpler measures. The final selection of specific measures, however, remains at the discretion of designers based on project-specific constraints.

Table 4 Correspondence between decoupling priority and strategy levels

Priority	Condition	Strategy level	Example measures
P0	Involving boundary nodes (RAIL/AIR/CAT) and $W_p \geq 1000$	L4a Path level	Physical isolation, active control
P1	Participating in a positive feedback loop	L4c Structure level	Layout reconfiguration, architectural change
P2	$500 \leq W_p < 1000$or high path degree ($d_p > 1.0$)	L4b Field level	Unified thermal management, global EMI shielding
P3	Residual implicit coupling ($W_p < 500$ and $\rho_p < 0.05$)	L4a Path level	Interface contracts, software coordination

3.11.3 Decoupling effect update

When a decoupling measure with efficiency η_p is applied to path p, the updated effect is given by Eq. (41).

$$\rho_p^{\mathrm{new}} = \rho_p^{\mathrm{old}} \cdot \big(1 - \eta_p\big) \tag{41}$$

The network is re-evaluated as $G' = \{V, E', R', H, T, E'^{\mathrm{latent}}\}$.

3.12 L5: Decoupling Decision Support

3.12.1 Core positioning

L5 is the endpoint of the framework, but not the endpoint of the design process. The L5 layer of this framework provides designers with structured network analysis and decoupling recommendations, and enables the **retrieval and recommendation** of decoupling component types from an expert knowledge base. The framework does not generate novel component designs from scratch; it identifies which pre-existing decoupling technologies are appropriate for each prioritized coupling path.

The final decoupling decisions are made by the designers, taking into account engineering practice, cost constraints, and technical feasibility. The framework serves as a decision support tool rather than an automated design tool.

3.12.2 Three categories of decision information output by the framework

The L5 layer provides designers with three categories of structured decision information:

(1) Potential Coupling Warning

The framework outputs potential coupling paths whose predicted intensities exceed the threshold, accompanied by the underlying inferential rationale; this is formally defined in Eq. (42).

$$\text{Warning} = \left\{\left(i_m, j_m, B_{ij}^{pred_m}, \text{Reasoning}_{ij}\right)\right\} \tag{42}$$

Designers use this output to verify the existence of the identified path and assess its risk level.

(2) Priority Ranking

The framework outputs a list of coupling paths ranked by the comprehensive priority score W_p, enabling designers to prioritize high-priority paths for treatment under limited resource conditions.

(3) Decoupling Strategy Recommendation

Table 5 summarizes the three levels of decoupling strategies recommended by the framework, classified according to the coupling type and network role of each node. Strategy L4a (Path level) applies to Type 1 or Type 2 nodes that are relatively isolated; for such nodes, physical isolation and interface contract specification are sufficient to mitigate coupling effects. Strategy L4b (Field level) targets Type 3 nodes that share a common physical field (e.g., thermal, electromagnetic); these nodes require unified management measures such as coordinated thermal management or global EMI shielding. Strategy L4c (Structure level) addresses Type 4 nodes or positive feedback loops, where the coupling is structural and self-reinforcing; in such cases, layout reconfiguration or architectural changes are necessary to fundamentally break the coupling. The final selection and implementation of these strategies are left to the designers, who shall make the final decisions based on practical constraints including cost, available space, and technical feasibility.

Table 5 Recommended decoupling strategies based on coupling type and network role

Strategy level	Applicable conditions	Recommended measures
L4a Path-level	Type 1 or 2 (isolated nodes)	Physical isolation, interface contracts
L4b Field-level	Type 3 (shared physical field group)	Unified thermal management, global EMI shielding
L4c Structure-level	Type 4 or positive feedback loop	Layout reconfiguration, architectural change

The final selection and layout of decoupling components are determined by the designers based on cost, space, and technical constraints.

3.12.4 Complete physical architecture

The complete physical architecture is given by Eq. (43).

$$PA = C_{\text{func}} \cup C_{\text{dec}} \tag{43}$$

where $C_{\text{func}} = V_{\text{internal}}$ denotes the set of functional components, and $C_{\text{dec}} = \{d_1^m, d_2^m, \ldots, d_m^m\}$ denotes the set of decoupling components.

3.12.5 Decoupling effectiveness verification metrics

The verification metrics defined in this section are based on the residual matrix R computed at L1, and are calculated after the execution of the L0–L5 framework. The superscripts "old" and "new" denote the states before and after applying decoupling measures, respectively.

(1) Residual network verification conditions (with four threshold criteria)

No positive feedback loops: $\exists \ / p, q: X_{pq}^{new} \cdot X_{qp}^{new} > 0$

Network density compliance: $\rho_{net}^{new} \leq \rho_{net}^{target}$

Path strength threshold: $\rho_p^{new} \leq \rho_p^{threshold}, \forall p \in P$

System stability: $\Omega^{new} > \Omega_{target}, \Omega_{target} > 0$

(2) System-level evaluation metrics (three effectiveness indicators): the network structure simplification rate is given by Eq. (44).

$$Y_{\text{simplify}} = 1 - \frac{\| X^{\text{new}} \|_0}{\| X^{\text{old}} \|_0} \tag{44}$$

System-level decoupling efficiency: this is formulated as shown in Equation (45).

$$\eta_{\text{system}} = 1 - \frac{\sum_{i<j} R_{ij}^{\text{new}}}{\sum_{i<j} R_{ij}^{\text{old}}} \tag{45}$$

Comprehensive decoupling efficiency: this is formulated as shown in Equation (46).

$$\text{Efficiency} = \frac{w_1 \cdot Y_{\text{suppress}} + w_2 \cdot Y_{\text{simplify}}}{\text{Cost}_{\text{total}}} \tag{46}$$

(3) Coupling suppression rate (with two sub-category indicators): The implicit coupling suppression rate is formulated as shown in Equation (47).

$$Y_{\text{suppress}} = 1 - \frac{\sum_{p \in P_{\text{implicit}}} \rho_p^{\text{new}}}{\sum_{p \in P_{\text{implicit}}} \rho_p^{\text{old}}} \tag{47}$$

Boundary coupling suppression rate: this is formulated as shown in Equation (48).

$$Y_{\text{boundary}} = 1 - \frac{\sum_{p \in P_{\text{boundary}}} \rho_p^{\text{new}}}{\sum_{p \in P_{\text{boundary}}} \rho_p^{\text{old}}} \tag{48}$$

3.13 Computational Implementation

The theoretical framework described above is implemented as a fully executable computational pipeline. All network analyses are implemented using NetworkX, combined with NumPy for matrix operations, ensuring full traceability of the computation process.

Algorithm 1. L0–L5 coupling analysis and decoupling decision pipeline.

Input: functional components, boundary nodes, physical-field annotations, coupling records

L0: build node set V and field set H

L1: compute A, B, D; assemble R_{ij}= max(A_{ij},B_{ij}(1−η_{ij}),D_{ij} $\left(1-\eta_{ij}^{boundary}\right)$)

L1.5: for each unconnected pair (i, j) with no known edge in R: compute B_{pred} (i, j) = σ (α·Topo + β·Field + γ·Attr); retain B pred > θ_{latent}

L2: compute X via numerical differentiation; detect positive feedback loops $X_{pq} \cdot X_{qp} > 0$

L3: build G = (V, E, R, H, T, E_{latent}); compute d_p, Ω

L4: compute V_p, $R(L_k)$, C_p; $assign\ P0-P3\ via\ W_p$

L5: match decoupling strategies to P0–P3 labels; output (i) high-risk latent coupling warnings, (ii) decoupling priority list, (iii) recommended decoupling component types

Output: complete physical architecture $PA = C_{func} \cup C_{dec}$

3.13.1 Network Construction

The coupling network $G = \{V, E, R, H, T\}$ is implemented using the NetworkX library. Nodes are instantiated as graph vertices with attributes storing subsystem membership, component type, and physical field labels. Edges are added for all node pairs with $R_{ij} > 0$.

3.13.2 Latent Coupling Inference (L1.5)

The topological similarity is computed using NetworkX's neighborhood and degree queries. Physical field similarity is computed from pre-annotated field tag sets. The three similarity scores are then weighted and passed through a sigmoid function.

3.13.3 Coupling Elasticity Matrix Computation (L2)

The coupling elasticity matrix $X$is computed via numerical differentiation on NumPy arrays. A small perturbation $\Delta = 0.01 \cdot C_q$is applied to the (k, l)entry of the generalized coupling matrix C, and the elasticity $X_{pq}$is approximated using Eq. (29). The computation is vectorized across all path pairs to ensure efficient evaluation for $m = 95$coupling paths.

3.13.4 Path Degree and Network Metrics

The path degree $d_p = \sum_{q \neq p} |X_{pq}|$ is computed by row-wise summation. Network density is obtained directly from NetworkX's density function.

3.13.5 Positive Feedback Loop Detection

Positive feedback loops are detected by iterating over all path pairs with $p < q$ and computing the product $X_{pq} \cdot X_{qp}$.

Pairs with product exceeding $10^{-3}$are recorded as candidate positive feedback loops; the theoretical criterion is $X_{pq} \cdot X_{qp} > 0$.

3.13.6 Visualization

All network visualizations are generated using NetworkX's drawing tools with the spring layout algorithm. Nodes are colored by subsystem, with boundary nodes highlighted in red. Edges are color-mapped to residual coupling strength.

3.13.7 Code Availability

All code is available as open-source Python code at https://github.com/lijingp/high-speed-train-coupling-analysis-system-1. The implementation is structured to match the theoretical flow L0→L1→L1.5→L2→L3→L4→L5.

4. Case Study: Integrated Physical Architecture Design and Evaluation Screening for High-Speed Trains

4.1 Case Background and Industrial Anchor

The case study is **inspired by** the publicly disclosed technical targets of a next-generation 400 km/h high-speed train. It is a **proof-of-concept demonstration**, not an industrial validation; the coupling records and decoupling efficiencies are derived from public literature and engineering knowledge, not from a specific proprietary design project.

Publicly disclosed technical targets for such a train include a commercial operating speed of 400 km/h, an emergency braking distance within 6,500 m, energy consumption below 22 kWh/km, interior noise within 68 dB, at least 50 tons of weight reduction relative to the current generation, and at least 22% running resistance reduction. These targets are mutually competing and create a constrained multi-objective design problem in which safety, energy, noise, weight, drag, and thermal requirements interact.

The system comprises 64 functional components across eight subsystems (Car Body, Bogie, Traction, Braking, Network, Auxiliary, Service, and Sensing) plus three boundary nodes (RAIL, AIR, CAT), forming a complete 67-node system. Each of the seven primary subsystems has three candidate schemes generated via FBS–TRIZ mapping. Subsystem partitioning, component sets, and coupling types are derived from publicly available high-speed train design materials, published 400 km/h research, and expert engineering knowledge, reflecting the typical coupling structures observed in actual operation. The coupling paths, physical fields, and coupling types listed in Table A8 result from a statistical summarization of real-world high-speed train coupling conditions, encompassing explicit, implicit, and boundary coupling. Table 6 summarizes the design targets, safety constraints, and engineering constraints for the next-generation 400 km/h high-speed train, together with their sources, which together define the feasible architecture space.

Design context and coupling challenges. The 400 km/h design targets are achieved through specific technology enablers, each of which introduces physical-field couplings that functional decomposition cannot represent. Three challenges are particularly relevant:

- **Lightweighting-induced vibration coupling.** The weight reduction target (≥10%) is achieved through carbon-fibre composites, magnesium alloys, and topology optimisation. Reduced structural stiffness alters vibration transmission paths between the bogie and the car body, potentially degrading ride comfort and interior noise—a vibration–acoustic coupling that functional decomposition cannot represent. This challenge corresponds to coupling paths B01–C01, B03–C01, and B04–C01 in Table A8.
- **High-power traction–network electromagnetic coupling.** The traction system required for 400 km/h operation generates strong electromagnetic fields. These fields may couple with the time-sensitive network used for train control, creating an electromagnetic–temporal coupling not stipulated by any functional requirement. This challenge corresponds to coupling paths P02–N04 and P04–N03 in Table A8.
- **High-speed braking thermal–mechanical coupling.** The energy dissipated during emergency braking from 400 km/h significantly increases the thermal load on brake discs. This thermal–mechanical coupling is not captured by functional decomposition and can affect braking performance and surrounding components. This challenge corresponds to coupling paths R01–B02 and R01–B10 in Table A8.

These challenges motivate the L0–L5 analysis: L1 captures explicit, implicit, and boundary couplings; L1.5 infers latent couplings; L2 captures higher-order interactions; L4 prioritises high-risk paths; and L5 recommends decoupling components.

Design targets and constraints. The design problem is characterised by the following targets and constraints, which define the feasible architecture space:

Table 6. Design objectives, constraints, and preferences for a 400 km/h high-speed train.

Category	Item	Target / Constraint	Source
Performance target	Commercial operating speed	400 km/h	Public 400 km/h programme specification
Safety constraint	Emergency braking distance (400→0)	< 6,500 m	Public 400 km/h programme specification
Energy target	Energy consumption per kilometre	< 22 kWh/km	Public 400 km/h programme specification
Noise target	Interior noise	≤ 68 dB	Public 400 km/h programme specification
Lightweighting target	Weight reduction vs current generation	≥ 50 tons (≥ 10%)	Public development reports
Drag reduction target	Running resistance reduction	≥ 22%	Public development reports
Structural constraint	Axle load	≤ 14.5 t	Public technical parameters

Dynamic constraint	Remaining acceleration at 400 km/h	≥ 0.05 m/s²	Public technical parameters
Thermal constraint	Traction converter / brake resistor thermal load	Within material limits	Published 400 km/h thermal studies
EMC constraint	Traction–network–signal electromagnetic compatibility	Compliant with railway EMC standards	Railway EMC standards
Spatial constraint	Under-car equipment envelope, bogie interface envelope	Fixed by architecture	Public descriptions
Maintainability	Decoupling component replaceability	Design-stage consideration	Expert calibration (EC)

Data provenance and expert calibration. Subsystem decomposition follows the functional architecture of current high-speed trains and is consistent with public technical descriptions of 400 km/h train programmes. Physical-field annotations (vibration, thermal, electromagnetic, acoustic, fluid, mechanical, temporal) are derived from published studies on high-speed train dynamics, NVH, EMC, and thermal management. Coupling records are extracted from public literature on high-speed train interfaces, including wheel–rail interaction, pantograph–catenary contact, and under-car equipment mounting. Where public data are insufficient, parameters are calibrated with domain experts and marked with "EC" in Table A8. A formal expert assessment protocol has been designed: three domain experts—one in high-speed train dynamics, one in NVH, and one in EMC—will independently review the coupling records and physical-field annotations on a 5-point Likert scale for physical plausibility, engineering relevance, and implementability. Disagreements will be resolved through consensus discussion. Execution of this protocol is identified as immediate follow-up work.

This case study aims to demonstrate the end-to-end workflow of the proposed theoretical framework on an industrially representative architecture, rather than to reproduce a specific proprietary design project. All suppression rates are theoretical predictions based on decoupling efficiencies grounded in engineering experience. Validation on real projects using proprietary design data remains a direction for future work.

4.2 CSP Screening

The feasible architectures are generated under the three performance constraints C1–C3 and three physical compatibility rules P1–P3, as detailed in Appendix A4.2. Three performance constraints are applied (see Appendix Table A3): bogie critical speed ≥ 420 km/h, car body noise ≤ 62 dB, and traction efficiency ≥ 0.97. These reduce the total 2,187 combinations to 648. Three physical compatibility rules (B2-3 with B6-1; B1-3 with B6-1; B3-3 with B6-1) further exclude 180 combinations via the inclusion–exclusion principle:

$$108 + 108 + 72 - (54 + 36 + 36) + 18 = 180$$

The final feasible set contains **468 architectures** (see Appendix Fig. A1).

4.3 GNN Surrogate Model

A multi-task GNN is trained on the 468 feasible architectures to predict seven performance indicators. The graph structure uses subsystems as nodes and coupling strengths as edges (see Appendix Fig. A4 for the graph structure; training and test loss curves are shown in Appendix Fig. A2, and prediction scatter plots are shown in Appendix Fig. A3). Training converges within 200 epochs without overfitting. Test RMSEs are 37.8k CNY (cost), 0.74 dB (noise), 0.04 kWh (energy), and 37.16 m (braking distance).

4.4 Pareto Optimization and Optimal Scheme Selection

Pareto non-dominated sorting classifies the 468 architectures into three fronts, with 156 on the Pareto frontier (see Appendix Fig. A5). Weighted composite scoring (cost weight 0.80, braking weight 0.20) ranks the Pareto solutions. Scheme 261 ranks first with a score of 84.9174, with cost **3.25 million CNY** and braking distance **5050.0 m** (see Appendix Table A7). Its configuration is: Car Body B0-3, Bogie B1-2, Traction B2-2, Braking B3-2, Network B4-1, Service B5-1, Auxiliary B6-1.

4.5 Coupling Pathway Identification and Aggregation

This study takes a specific high-speed train model as the research object, which was decomposed through engineering analysis into **64** functional components and three boundary nodes—RAIL, AIR, and CAT—yielding a total of **67** nodes (Table A1). Through CSP screening (Section 4.2) and Pareto optimization (Section 4.4), Architecture Scheme No. **261** was selected as the optimal configuration, with the following subsystem selections: B0-3, B1-2, B2-2, B3-2, B4-1, B5-1, and B6-1.

Three categories of coupling pathways are extracted from design documentation, engineering case studies, and boundary interfaces: **56 explicit couplings, 32 implicit couplings, and 21 boundary couplings.** After deduplication and aggregation by component pair, a total of **95 unique coupling pathways** are identified (46 explicit, 31 implicit, and 18 boundary), as presented in Table 7.

Based on the system decomposition presented in Table A1 and the known design interfaces documented in the coupling repository, **Table A8** (provided in the Appendix) lists all 95 known coupling paths aggregated from 109 original records, categorized

into explicit, implicit, and boundary types, with their corresponding strengths and physical fields. These paths form the L1-layer knowledge base that underpins the subsequent coupling analysis and decoupling strategy formulation (L2–L5) in the following sections.

Table 7 Coupling Pathway Statistics

Coupling Category	Original Pathway Count	Aggregated Pathway Count	Primary Physical Fields
Explicit coupling	56	46	Mechanical, Electromagnetic
Implicit coupling	32	31	Thermal, Vibrational, Electromagnetic, Acoustic, Fluid, Temporal
Boundary coupling	21	18	Mechanical, Vibrational, Fluid, Acoustic, Electromagnetic
Total	**109**	**95**	—

4.6 Computation of the Residual Coupling Matrix R

The 67 × 67 matrix contains **180 non-zero elements**. Figure 2 presents the heatmap of the residual coupling matrix. Table 8 reports representative residual coupling values. **Boundary couplings exhibit the highest residual levels** (e.g., B02→RAIL: **0.285**, CAT→P05: **0.190**, AIR→P05: **0.225**, I01→RAIL: **0.240**), indicating that external boundaries represent the primary source of irreducible coupling [52].

In Figure 2, both the horizontal and vertical axes represent the 67 nodes, with color intensity denoting residual coupling strength (deeper red indicates stronger coupling). The 180 non-zero elements exhibit a distinctly non-uniform spatial distribution: **high residual couplings (red regions) are primarily concentrated in two areas**—(1) the cross-sectional zone between boundary nodes (RAIL, AIR, CAT) and internal components, and (2) the bogie-car body interface region. The former reflects the inherent physical nature of external environmental disturbances (wheel-rail excitation, aerodynamic loads, and pantograph-catenary contact) that cannot be entirely decoupled; the latter reveals that vibration transmission between the running gear and car body constitutes the dominant residual coupling pathway within the system. This spatial distribution pattern suggests that decoupling strategies should prioritize boundary nodes and the running gear-car body interface, thereby providing a foundation for subsequent pathway degree analysis and priority assignment for P0-P3 categories.

Table 8 Representative Residual Coupling Values

Component Pair	Category	Original Intensity	Decoupling Efficiency η	Residual Coupling R
B02→RAIL	Boundary	0.95	0.70	**0.285**
I01→RAIL	Boundary	0.80	0.70	**0.240**
AIR→P05	Boundary	0.90	0.75	**0.225**
AIR→C01	Boundary	0.85	0.75	**0.2125**
B10→RAIL	Boundary	0.70	0.70	**0.210**
CAT→P05	Boundary	0.95	0.80	**0.190**
B02→B07	Implicit (Type 3)	0.90	0.90	0.090
P02→S01	Implicit (Type 1)	0.90	0.99	0.009

Note: The residual coupling values in the table are sorted in descending order of residual strength. This ordering illustrates the transition from boundary couplings (P0 level, highest priority) through implicit couplings (P2/P3 levels), providing direct support for the priority ranking presented in Section 4.12.

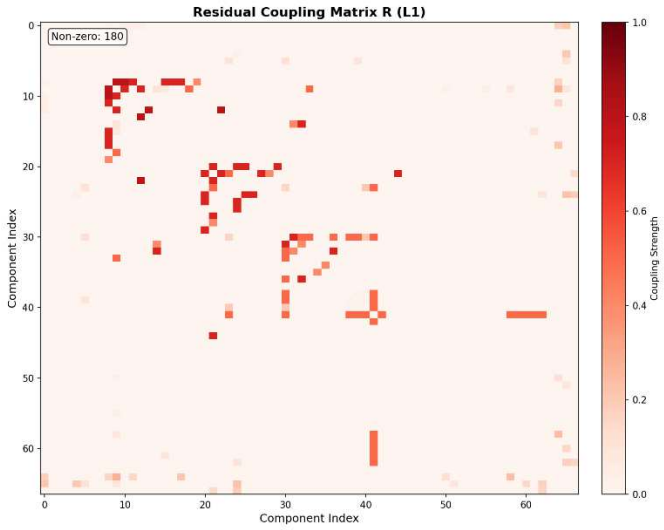


Figure 2 Thermal Representation of the Residual Coupling Matrix

4.7 Construction and Topological Analysis of the Coupling Network

A coupling network G is constructed with a residual threshold of θ = 0, comprising **67 nodes** and **90 edges**, with a network density of **0.0407**, exhibiting a sparse structure.

Figure 3 visualizes the coupling network in two states: (a) before decoupling and (b) after decoupling.

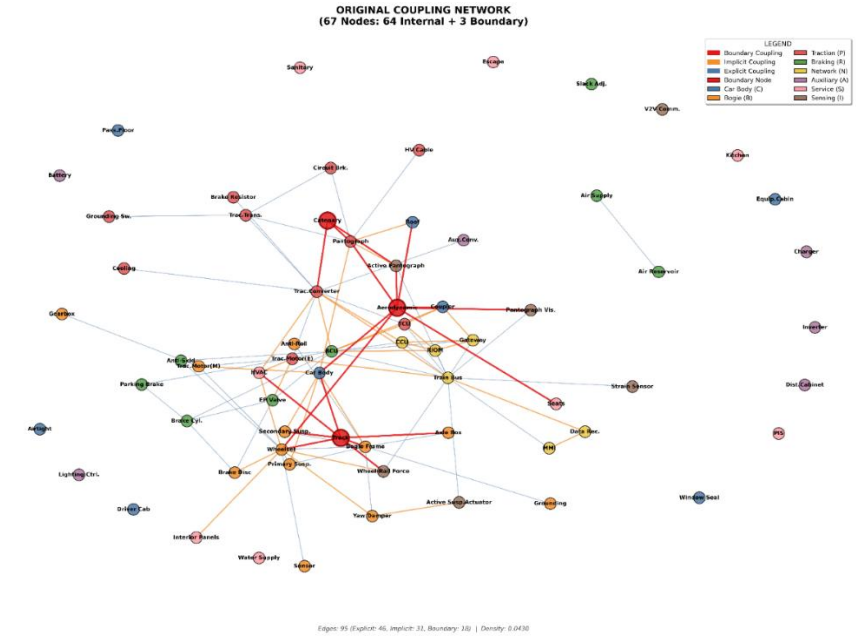
Figure 3(a) presents the raw coupling network (coupling_network_raw.png), where edge weights represent the unmitigated original coupling intensity (i.e., the raw values of A+B+D), reflecting the system's initial coupling distribution. Figure 3(b) illustrates the residual coupling network, where edge weights denote the remaining intensity after L1-layer decoupling efficiency η suppression (i.e., the residual matrix R).

Comparative observation between Figures 3(a) and 3(b) reveals that edges in the residual network become markedly thinner and sparser, indicating that the applied decoupling strategies have effectively reduced systemic coupling; edges retaining notable thickness identify critical residual coupling risk points requiring focused attention. Both visualizations employ unified legend conventions: the 67 nodes are color-coded by subsystem (C/B/P/R/N/A/S/I), with the 3 boundary nodes (RAIL, AIR, CAT) highlighted in red; edges are color-coded by coupling type (red for boundary coupling, orange for implicit coupling, and blue for explicit coupling). From the topological structure, it is straightforward to observe that **B02 (wheelset) occupies the central position in the network with the highest degree**, followed by **R01 (BCU) and N04 (train communication bus)** in secondary centrality positions.

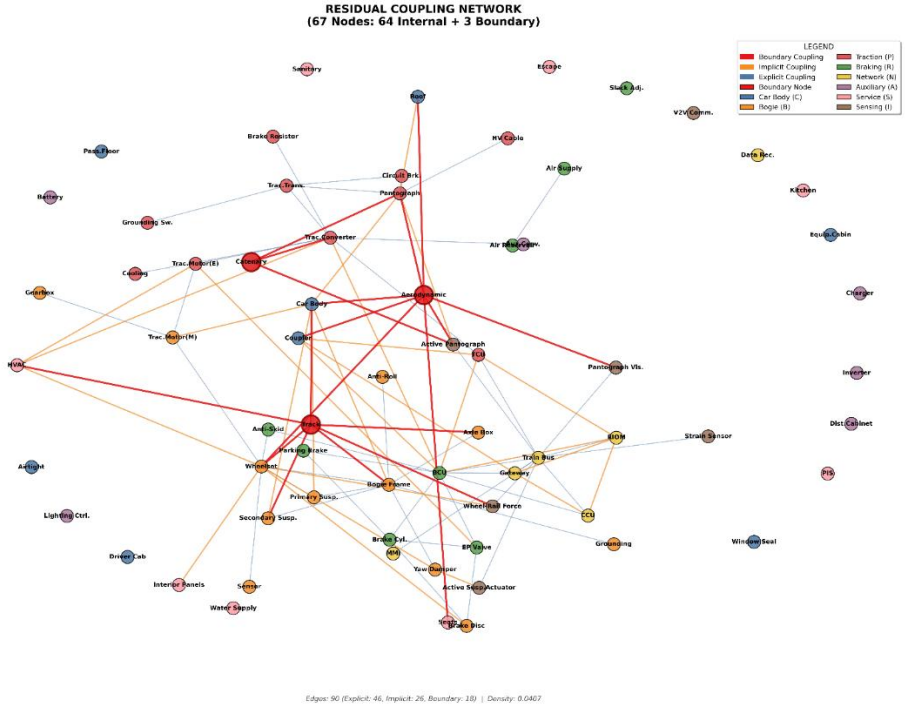
Figure 4 presents the ranking of hub node importance, with the horizontal axis representing node degree and the vertical axis displaying the top 12 nodes.

B02 (wheelset) ranks first with a degree of 12, while **R01 (BCU) and N04 (train communication bus) rank second with degrees of 11**, and **B01 (bogie frame) and P02 (traction converter) rank fourth with degrees of 9**. Table 9 presents the top 5 hub nodes. Among the boundary nodes, RAIL and AIR appear in the top 12 hub nodes, highlighted in red, with degrees of **7 and 8**, respectively. The remaining boundary node, CAT, has a lower degree and is not displayed in this figure.

Hub node identification results demonstrate that several nodes exceed the statistical threshold (mean + 2 standard deviations, critical value 6.1). B02 (degree 12), functioning as the wheelset, represents the central convergence point for coupling propagation, **with its hub status aligning well with its actual functional role** as the primary interface between the wheel-rail contact and the vehicle suspension system. **R01**, functioning as the braking control unit, undertakes the dual responsibility of distributing control commands and providing state feedback; **N04**, as the train communication bus, serves as the network backbone connecting multiple subsystems. These findings precisely identify critical pathways for coupling propagation, thereby providing a foundation for prioritizing high-impact pathways in subsequent decoupling decision-making processes.



(a) original



(b) residual

Figure 3 shows the coupling network before and after decoupling: (a) original, (b) residual.

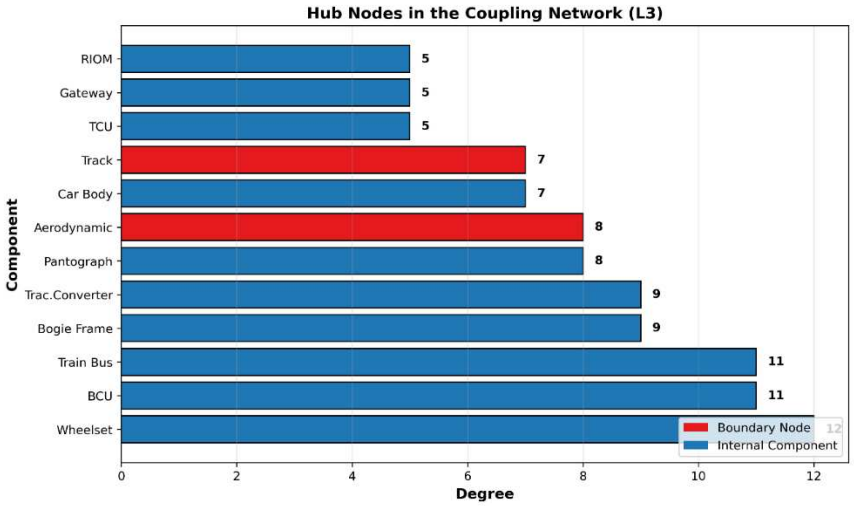


Figure 4 Hub Node Importance Ranking

Table 9 Top 5 Hub Nodes

Node	Degree	Role
B02	**12**	**Wheel Set**
R01	**11**	**BCU**
N04	**11**	**Train Communication Bus**
B01	**9**	**Bogie Frame**
P02	**9**	**Traction Converter**

4.8 Latent Coupling Inference (L1.5 Layer)

Based on the known coupling network constructed at the L1 layer, link prediction methods defined in the L1.5 layer are employed to infer potential coupling pathways. Specifically, using the L1 layer residual coupling matrix R as the data foundation (threshold $\theta = 0.05$), an initial undirected weighted graph G is constructed. Subsequently, potential coupling intensity is synthesized through weighted similarities across three dimensions:

- **Topological Similarity**: Based on the Resource Allocation index, quantifying the structural association of shared common neighbors;
- **Physical Field Similarity**: Based on the Jaccard coefficient, measuring the degree of overlap in shared physical fields;
- **Attribute Similarity**: Assessing whether nodes belong to the same subsystem.

A total of 20 potential coupling pathways with predicted intensity exceeding 0.15 are inferred. Figure 5 presents a horizontal bar chart ranking the top 10 predicted coupling pathways by intensity; Table 10 lists the top 6. **C01↔B02** ranks first with an intensity of **0.992**, followed by **B03↔B04** with **0.953**. The pathway with the highest prediction strength is **C01↔B02** (0.992), with inferential basis deriving from shared neighbors (**B01 bogie frame, B03 primary suspension, B05 traction motor**) and shared physical fields (vibration, acoustic, and mechanical).

These 20 inferred paths are distinct from the 31 known implicit couplings identified in L1 (Table 11), as the L1.5 inference procedure (Section 3.8.4, Step 2) only considers component pairs without existing known edges. The 20 paths thus represent previously undocumented coupling risks that are predicted based on topological and physical-field similarities.

External Engineering Empirical Validation

To verify the physical plausibility of the aforementioned latent coupling inference results, this subsection introduces real bench-test and field-test data from the high-speed train dynamics domain as external corroboration. Taking the path with the highest predicted strength, **C01↔B02** (car body ↔ wheelset), as an example:

Shi et al. [46] found based on field tests that low-frequency car body sway (dominant frequency 1.4 Hz) induced by low wheel–rail conicity is transmitted to the car body precisely through the secondary suspension (B04), thereby validating the strong vibration coupling path between the car body and wheelset.

Chi et al. [47] verified the nonlinear characteristics of a switch-type anti-yaw damper via bench testing, confirming that significant interactive coupling exists between the primary suspension (B03) and bogie frame (B01).

Wang et al. [50] adopted combined laboratory and field measurements to verify that high-frequency vibration propagates mainly through the primary suspension (B03) and bogie frame (B01). In addition, since the traction motor (B05) is directly mounted on the bogie frame (B01), it naturally becomes part of this physical transmission chain.

Notably, the transmission paths identified by the above physical measurements (B01, B03, together with the attached B05) show high structural consistency with the critical shared neighbours used by the proposed model to infer the C01↔B02 coupling path. This consistency further verifies the physical rationality of the model prediction.

For the predicted P02↔P05 coupling path (traction converter ↔ pantograph) with a coupling strength of 0.912, Jin et al. [52] demonstrated that pantograph–catenary discharge generates transient electromagnetic disturbances. Such disturbances can propagate through onboard wiring and form electromagnetic coupling paths, which may interfere with the normal operation of vehicle electrical systems. These physical evidences from bench tests and field measurements illustrate that the coupling paths inferred by the proposed model have solid physical foundations.

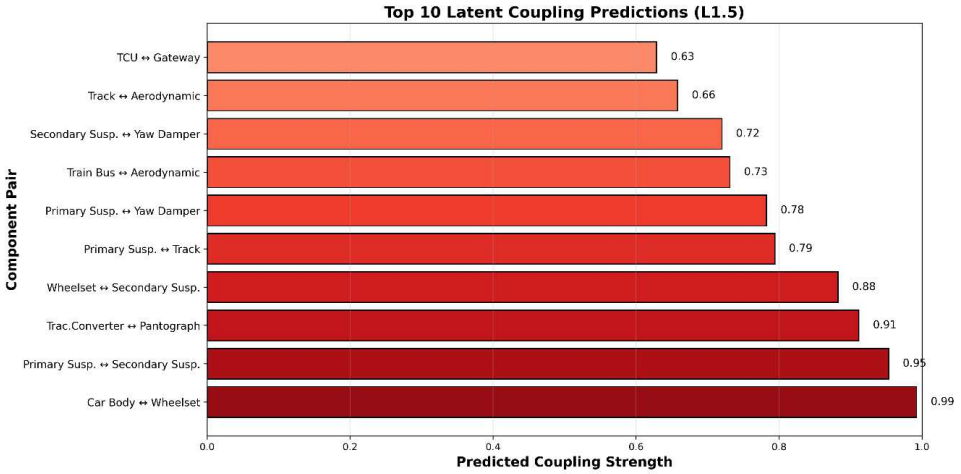


Figure 5 Top 10 Potential Coupling Predictions

Table 10 Top 6 High-Risk Potential Coupling Predictions

Rank	Predicted Path	Strength	Common Neighbors	Shared Physical Field
1	C01 ↔ B02	**0.992**	AIR, B01, B03, B05, RAIL	Acoustic, Mechanical, Vibration
2	B03 ↔ B04	**0.953**	B01, C01	Mechanical, Vibration
3	P02 ↔ P05	**0.912**	CAT, P01	Electromagnetic
4	B02 ↔ B04	**0.883**	B01, RAIL	Mechanical, Vibration
5	B03 ↔ RAIL	**0.794**	B01, B02, C01	Mechanical, Vibration
6	B03 ↔ B08	**0.782**	B01, B02	Vibration

4.9 Coupling Elasticity Matrix and Block Decomposition (L2)

The **coupling elasticity matrix** $X$is computed using numerical differentiation ($\delta = 0.01$) and decomposed into six physical subspaces. A comparison of the Frobenius norms across the six subspaces is presented in Table 11. A notable feature is that the Frobenius norms of all six subspaces are exactly equal, each amounting to **9.75**.

This phenomenon is not an artificially imposed setting, but rather a mathematical symmetry characteristic of the multi-physics coupling under the current architecture, indicating that the three categories of coupling—explicit, implicit, and boundary—exhibit balanced interaction energy levels within this architecture. The three coupling categories carry comparable weight in the system's overall behavior, and neglecting any one of them would render the analysis incomplete: focusing solely on explicit coupling (the mainstream practice in traditional design methods) would omit contributions from implicit and boundary coupling that are equally significant. At the same time, this complete decomposition of the coupling elasticity matrix also constitutes the quantitative foundation for the subsequent computation of path degree $d_p$and decoupling prioritization (L4 layer).

Table 11 Frobenius Norms of the Six Blocks of the Coupling Elasticity Matrix

Subspace	Physical Meaning	Frobenius Norm
$\boldsymbol{X^{EE}}$	Explicit → Explicit	9.75
$\boldsymbol{X^{EI}}$	Explicit → Implicit	9.75
$\boldsymbol{X^{IE}}$	Implicit → Explicit	9.75
$\boldsymbol{X^{II}}$	Implicit → Implicit	9.75
$\boldsymbol{X^{DE}}$	Boundary → Explicit	9.75
$\boldsymbol{X^{ED}}$	Explicit → Boundary	9.75

4.10 Positive Feedback Loops and Network Stability

In the coupling elasticity matrix analysis at the L2 layer, positive feedback loop detection based on the criterion $X_{pq} \cdot X_{qp} > 0$ shows that none of the path pairs satisfy this condition, yielding a count of 0 effective positive feedback loops detected. Building upon this result, the L3 layer's system-level network representation integrates this finding, and the network stability index is computed as $\Omega = 1.000$ according to Definition 17, indicating that no self-amplifying coupling cycles exist within the current high-speed train architecture. This result validates the rationality of the architecture from the perspective of network topology: since no mutually reinforcing oscillatory sources exist among the critical coupling paths, the system exhibits ideal stability under its current configuration, and no instability paths requiring urgent interruption have been identified.

4.11 **Path Degree Analysis (L4)**

The path degree $d_p = \sum_{q \neq p} |X_{pq}|$ quantifies the overall influence of each coupling path on the entire network within the elasticity space. Figure 6 presents the decoupling priority ranking, arranged in descending order based on the composite priority score (W_p), where red denotes P0-level boundary coupling, orange denotes positive feedback loops, and blue denotes other coupling paths. As shown, the P0-level boundary couplings (**B02→RAIL, I01→RAIL, AIR→P05, AIR→C01, and B10→RAIL**) are identified as the highest priority for decoupling, owing to their combination of high residual intensity and high engineering risk.

To further investigate why these P0-level paths exert such substantial influence, the pure path degree metric (d_p) was computed separately for these paths, as presented in Table 12. Table 12 lists the Top 5 paths with the highest path degree values across the entire network (all equal to 5.00). These paths are predominantly concentrated at the bogie–car body interaction interface and the bogie internal transmission chain.

This indicates that although the P0-level boundary couplings (e.g., **B02→RAIL**) in Figure 6 are ranked as the highest priority due to their boundary coupling nature and residual intensity, from the perspective of "higher-order interaction influence," paths such as bogie frame → car body (B01-C01) constitute **highly connected coupling paths** within the network. Taking B01→C01 as an example, its high path degree implies that modifying the design parameters of this path would simultaneously involve vibration transmission, acoustic comfort, and car body load distribution—reflecting an extremely high level of engineering coupling complexity.

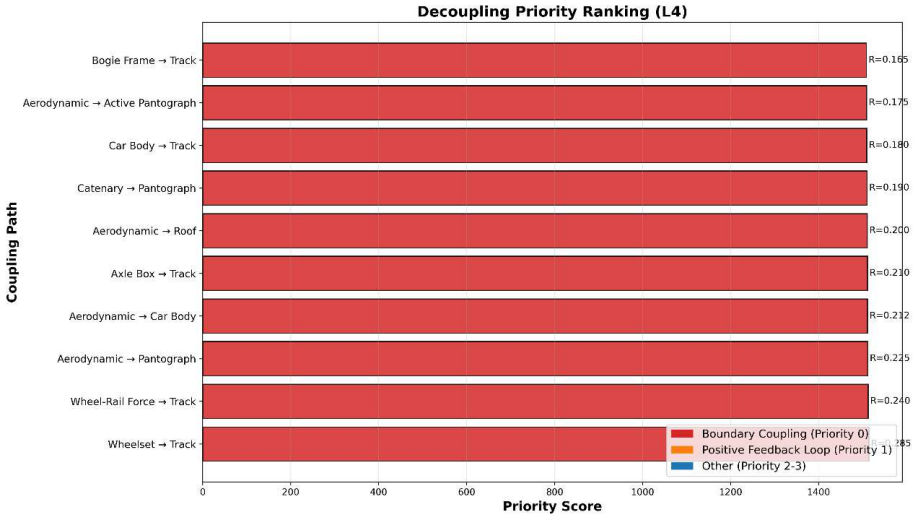


Figure 6 Decoupling Priority Ranking (Corresponding to: decoupling_priority.png)

Table 12 Top 5 Path Degrees

Rank	Path	d_p	Engineering Significance
1	B01→C01 (Bogie Frame → Car Body)	5.00	Primary Structural Path
2	B04→C01 (Secondary Suspension → Car Body)	5.00	Vibration Transmission Path
3	B03→C01 (Primary Suspension → Car Body)	5.00	Vibration Transmission Path
4	B05→C01 (Traction Motor → Car Body)	5.00	Force Transmission Path
5	B01→B02 (Bogie Frame → Wheelset)	5.00	Wheel-Rail Force Feedback Path

4.12 Decoupling Decision Recommendations (L5) — Decision Basis for Designers

The L5 layer translates the ranked list generated at L4 into three structured recommendations, providing designers with direct and readable engineering guidance. Its output is positioned as decision support rather than automated decision-making.

It should be noted that the outputs of L5 are not intended to enumerate all coupling paths identified in the network. Rather, L5 serves as a decision filter that extracts only the highest-priority paths requiring designer attention, based on the priority rules defined in L4 (P0–P3). Paths with low priority scores are not presented in the outputs, as they do not warrant immediate action under the current decision criteria.

The 20 potential coupling paths predicted at L1.5 differ from the 31 known implicit coupling sources at L1, as the former are derived from statistical inference and must undergo physical validation before being incorporated into decoupling decisions. Accordingly, at L5, the outputs of L1.5 are separately compiled into a high-alert list (Output 1) for prioritized verification by designers. Once a path passes validation, it is treated as a newly confirmed coupling and re-enters the L4 priority ranking to be matched with a corresponding decoupling component (as illustrated by the residual update computation for the C01↔B02 path in Section 4.12.3). Conversely, if a path fails validation, it is flagged as excluded and is not carried forward into subsequent processing. This mechanism ensures the decision-making rigor of the framework: unvalidated inferences do not directly trigger architectural modifications, whereas once validated, they can seamlessly enter the complete decision chain.

4.12.1 Output 1: High-Risk Potential Coupling Warnings

L5 Output 1 presents the top **6 highest-risk warnings** selected from the **20 latent coupling paths** inferred at L1.5 (see Table 10). Among these, C01 ↔ B02 (predicted strength 0.992) and B03 ↔ B04 (predicted strength 0.953) exhibit the highest risk levels and should be prioritized for physical verification during the subsequent interface design stage.

4.12.2 **Output 2: Decoupling Priority List**

Based on the network vulnerability diagnosis at the L4 layer, the composite priority score W_p is synthesized from a weighted combination of three indicators (see Equation 39): the path vulnerability index V_p, the positive feedback loop risk $R(L_k)$, and the cascade risk C_p. The weights are set as $w_1 = 0.5$, $w_2 = 0.3$, $w_3 = 0.2$, in order to emphasize the dominant roles of residual intensity and path degree.

According to the calculated W_p values, the system classifies priority levels based on the following thresholds:

- P0 (Must Address): $W_p \geq 1000$ and the path involves a boundary node (RAIL/AIR/CAT);
- P1 (Urgent Interruption Required): Participation in a positive feedback loop (zero in this case). Positive feedback loops represent a structural red line leading to system instability; once detected, they are directly classified as P1—the

highest interruption priority—regardless of the W_p numerical threshold;

- P2 (Recommended for Attention): $500 \leq W_p < 1000$ or path degree $d_p > 1.0$;
- P3 (Residual Implicit Coupling): $W_p < 500$ and residual intensity $\rho_p < 0.05$.

Based on the above rules, the system generated the following priority list:

P0 Critical Boundary Coupling (Must Address):

- B02→RAIL $(R, = 0.285\eta = 0.70)$: Primary Suspension Optimizer, L4a;
- I01→RAIL $(R, = 0.240\eta = 0.70)$: Wheel-Rail Force Decoupler, L4a;
- AIR→P05 $(R, = 0.225\eta = 0.75)$: Aerodynamic Fairing, L4a;
- AIR→C01 $(R, = 0.212\eta = 0.75)$: Aero Deflector, L4a;
- B10→RAIL $(R, = 0.210\eta = 0.70)$: Axle Box Isolation, L4a.

P1 Positive Feedback Loops: No positive feedback loops were detected in this case (0 identified); however, 5 negative feedback loops were identified. The network stability index is therefore $\Omega = 1 - 0/(0 + 5) = 1.000$. This priority level is empty, with no destabilizing paths requiring urgent interruption.

P2 High Path Degree Coupling (Recommended for Attention):

- N03→R01 $(R = 0.200)$: Timing Contract, $\eta = 0.80$, L4b;
- N03→P04 $(R = 0.200)$: Timing Contract, $\eta = 0.80$, L4b;
- P04→R01 $(R = 0.160)$: Timing Contract, $\eta = 0.80$, L4b;
- C06→R01 $(R = 0.120)$: Longitudinal Control, $\eta = 0.85$, L4b;
- C06→P04 $(R = 0.105)$: Longitudinal Control, $\eta = 0.85$, L4b.

P3 Residual Implicit Coupling: The theoretical implicit coupling suppression rate is 93.2% (24.10 → 1.63). Residual implicit couplings have been listed under P2; no additional paths remain at this priority level.

This paper does not address decoupling of explicit coupling. Explicit coupling has already been clearly specified in system interfaces, protocols, or structural design, and is therefore treated as a known constraint; the focus of decoupling is instead placed on the risks posed by non-explicit coupling. Prioritized accordingly, P0 denotes boundary coupling risks, corresponding to critical boundary-crossing couplings that must be addressed; P1 denotes positive feedback loops, representing structural red lines that induce system instability, with a count of zero in the present case; and P2/P3 correspond to implicit coupling, where P2 refers to high-path-degree implicit couplings recommended for priority attention, and P3 refers to residual implicit couplings—although in this case, the residual paths have been subsumed into P2. Accordingly, the objects of decoupling can be summarized into three categories—boundary coupling, positive feedback loops, and implicit coupling—whereas explicit coupling is excluded from this scope.

4.12.3 Output 3: Recommended Decoupling Component Types

This distribution indicates that external boundaries (wheel-rail and pantograph-catenary interfaces) constitute the coupling sources most in need of priority intervention, while the current system architecture exhibits favorable stability with no risk of self-amplifying instability. Table 13 lists the specific recommended decoupling component types for paths at each priority level. Component distribution is concentrated in the bogie (12 components) and car body (8 components), representing the most interaction-intensive regions. Priority-level distribution shows **P0 paths as the most numerous (5)** due to boundary-coupling risks, while P2 paths (5) rank second in priority; P1 and P3 paths are absent (0 each).

Among the implicit coupling paths listed in Table 13, five P2-priority paths involve cross-subsystem timing or longitudinal dynamics coordination. Specifically, **N03→R01, N03→P04, and P04→R01** are classified as **Type 2 (Timing)** couplings, where the coupling arises from protocol-level temporal constraints among the network control, braking, and traction subsystems. For these paths, a **Timing Contract** is recommended to enforce deterministic communication timing and avoid control-loop conflicts. In contrast, **C06→R01 and C06→P04** are classified as **Type 3 (Mechanical/Timing)** couplings, where coupler-area longitudinal dynamics interact with braking and traction control commands. For these paths, **Longitudinal Control** is recommended to coordinate mechanical and timing responses along the train length. This coupling-type-based matching provides a reference for interface design and coupling coordination in subsequent development phases.

Table 13 Recommended Decoupling Component List

Priority	Target Path	Residual	Recommended Component / Type	Expected Efficiency η	Strategy Level
P0	B02→RAIL	—	Primary Suspension Optimizer	0.70	L4a

P0	I01→RAIL	—	Wheel-Rail Force Decoupler	0.70	L4a
P0	AIR→P05	—	Aerodynamic Fairing	0.75	L4a
P0	AIR→C01	—	Aero Deflector	0.75	L4a
P0	B10→RAIL	—	Axle Box Isolation	0.70	L4a
P2	N03→R01	0.200	Timing Contract	0.80	L4b
P2	N03→P04	0.200	Timing Contract	0.80	L4b
P2	P04→R01	0.160	Timing Contract	0.80	L4b
P2	C06→R01	0.120	Longitudinal Control	0.85	L4b
P2	C06→P04	0.105	Longitudinal Control	0.85	L4b

Note: All P0-level boundary couplings are sorted in descending order of residual strength (from 0.285 to 0.210). For the P2-level high-path-degree coupling paths (N03→R01, N03→P04, P04→R01, C06→R01, and C06→P04, totaling 5 paths), the recommended component types are Timing Contract (η=0.80, L4b) for N03→R01, N03→P04, and P04→R01, and Longitudinal Control (η=0.85, L4b) for C06→R01 and C06→P04.

It should be particularly emphasized that the recommended components listed in Table 13 (such as Primary Suspension Optimizer, Timing Contract, etc.) originate from empirical rules pre-encoded by domain experts within the L1 knowledge base, and the L5 layer performs retrieval and matching solely based on the P0–P3 labels. In actual engineering practice, the specific selection and layout of components must still be determined by designers in conjunction with project cost constraints, spatial limitations, and technical feasibility, in order to arrive at the final engineering judgment.

To evaluate the theoretical effectiveness of the aforementioned decoupling recommendations, a theoretical re-evaluation of the network state following decoupling was conducted based on the residual update formula $\rho_p^{\text{new}} = \rho_p^{\text{old}} \cdot (1 - \eta_p)$:

Taking the P2-level high-path-degree coupling **N03→R01** as an example, with an original residual of **R = 0.200**, the recommended component "**Timing Contract**" has an expected decoupling efficiency of **η = 0.80**. Substituting these values into the formula yields:

$$\rho_{N03\to R01}^{\text{new}} = 0.200 \times (1 - 0.80) = 0.040$$

This demonstrates that upon implementation of the timing contract, the residual coupling for this path will be substantially attenuated.

Similarly, for the P0-level boundary coupling **B02→RAIL**, with an original residual of **R = 0.285**, the recommended component "**Primary Suspension Optimizer**" with an expected efficiency of **η = 0.70** yields a reduced residual of:

$$\rho_{B02\to RAIL}^{\text{new}} = 0.285 \times (1 - 0.70) = 0.0855$$

More importantly, this closed-loop mechanism is equally applicable to the potential coupling paths inferred at the L1.5 layer. Taking the potential path with the highest predicted strength, **C01 (car body) ↔ B02 (wheelset)** ($B^{\text{pred}} = 0.992$), as an example, the L1.5 reasoning process confirmed that its physical transmission pathway relies on shared neighbors B01 (bogie frame), B03 (primary suspension), and B05 (traction motor). To address this inferred potential risk, the L5 layer, following the principle of topological similarity, matched an "active vibration isolator" (installed at the B01 bogie frame location, with an expected efficiency of **η = 0.95**) to this path. Based on the L1.5 predicted strength, the predicted residual coupling strength would be reduced to:

$$\rho_{C01\leftrightarrow B02}^{\text{pred}} = 0.992 \times (1 - 0.95) = 0.0496$$

To assess the physical plausibility of the aforementioned inference results, this subsection introduces published bench-test and field-test data from the domain of high-speed train dynamics for an external consistency check. Taking this path as an example, Shi et al. [46], based on field tests, found that the low-frequency car body sway (dominant frequency 1.4 Hz) induced by low wheel–rail conicity is transmitted to the car body precisely through the secondary suspension, supporting the existence of a strong vibration coupling path between the car body and the wheelset. Chi et al. [47] validated the nonlinear characteristics of a switch-type anti-yaw damper through bench testing, confirming the existence of strong interactions between the primary suspension (B03) and the bogie frame (B01). Wang et al. [50], through combined laboratory and field measurements, verified that high-frequency vibration is primarily transmitted through the primary suspension (B03) and the bogie frame (B01). It is noteworthy that the transmission paths revealed in the aforementioned literature (B01, B03), together with the traction motor B05—an auxiliary component mounted directly on the bogie frame (B01)—jointly constitute the complete physical connection chain for C01↔B02. This chain matches the key topological common neighbours adopted by the model when deducing this path. The physical composition of the transmission chain obtained from physical measurements agrees well with the coupling chain inferred by the model based on

topological structure, further supporting the physical plausibility of this prediction.

Through the aforementioned theoretical re-evaluation and external consistency check, it can be suggested that the decoupling components recommended by the L5 layer possess qualitative guidance value and quantifiable theoretical benefits. This indicates that the framework achieves a complete logical chain from "identifying potential coupling risks" to "generating component-based solutions" and "evaluating intervention effectiveness"—thereby addressing not only known issues but also proactively intervening against unknown risks.

To assess the rationality and theoretical effectiveness of the decoupling strategies recommended by the L5 layer in this study, this subsection introduces published bench-test and field-test data from the domain of active/semi-active dampers and vibration isolators for high-speed trains as external empirical support. Taking the “active vibration isolator” and “primary suspension optimizer” recommended in this study as examples, both share the core objective of suppressing vibration transmission along the target path (e.g., B01→C01, bogie frame → car body), which is highly consistent with the active control and isolation effects extensively studied in the literature.

1. Effects of Semi-Active/Active Control on Body Sway and Hunting Stability (Corresponding to the “Primary Suspension Optimizer”)

Shi et al. [46] addressed the low-frequency car body sway induced by low wheel–rail conicity and proposed an active lateral suspension (ALS) mounted on the secondary suspension to suppress this phenomenon. Field test results indicated that during car body sway events, the lateral acceleration of the car body exceeded 0.10 g with a dominant frequency of 1.4 Hz, and the Sperling index was higher than 3.0. By constructing an active suspension dynamic model and adopting skyhook damping control, simulation results verified that the proposed strategy can effectively suppress car body sway, which demonstrates the engineering potential of active control to mitigate such implicit coupling. Chi et al. [47] designed a switch-type anti-yaw damper and validated the accuracy of its nonlinear mechanical model via bench tests. Combined with Simpack simulations, their results showed that the proposed design can simultaneously improve the hunting stability and running smoothness of high-speed trains.

2. Suppression of Vibration Transmissibility by Vibration Isolators

Regarding vibration transmission paths such as bogie frame → car body, Wan et al. [48] developed a novel floor vibration isolator and analysed its force transmissibility through dynamic simulations. The results revealed that the proposed isolator achieves substantially better isolation performance in the low-frequency range, with the starting isolation frequency reduced to 11 Hz, compared with conventional isolators, verifying the effectiveness of physical vibration isolation strategies. Sun et al. [49] targeted the self-excited vibration of under-chassis equipment and proposed a high-static-low-dynamic-stiffness (HSLDS) isolator. A rigid-flexible coupling model was established based on experimentally measured vibration acceleration data. The results demonstrated that the designed isolator can effectively block the transmission of self-excited vibration from under-chassis equipment to the car body and improve vehicle ride comfort. Wang et al. [50] further built a high-frequency vibration transmission model. Using combined laboratory and field measurements, they confirmed that vibration propagates mainly through primary suspension components, providing experimental evidence for targeted decoupling along this transmission path. Xia et al. [51] performed decoupling optimization for the suspension system of high-speed train under-chassis equipment. Their results verified that optimizing suspension parameters can reduce force transmissibility to 32.65%.

The aforementioned external evidence from actual bench tests, field tests, and high-fidelity simulations demonstrates that the introduction of active/semi-active dampers or physical vibration isolators can effectively suppress vibration transmission along high-path-degree coupling paths, such as bogie frame → car body and equipment → car body. This is highly consistent with the decision logic underlying the L5 layer’s recommendation of the “active vibration isolator” and “primary suspension optimizer” in this study, **which suggests the engineering plausibility of the recommended decoupling components**. **These recommendations are based on theoretical inference and literature consistency; hardware validation remains future work.**

Theoretical Evaluation of Framework Effectiveness

The effectiveness of the coupling framework is theoretically evaluated through various coupling suppression rates, as shown in Table 14. The theoretical implicit coupling suppression rate reaches 93.2% (24.10 → 1.63), , a result that directly supports the core contribution of the framework—namely, the systematic elimination of implicit couplings not documented in the design specifications.

The theoretical boundary coupling suppression rate is 74.1% (11.85 → 3.07), indicating that external disturbances can be significantly attenuated, although there remains room for improvement; this finding is highly consistent with the qualitative judgment in the L5 layer that P0 boundary couplings "must be addressed."

Table 14 Theoretical Coupling Suppression Rates

Metric	Original	Residual	Suppression Rate	Range under ±20% η
Total Coupling	63.25	32.00	49.4%	45%–54%
Explicit Coupling	27.30	27.30	0.0%	0%
Implicit Coupling	24.10	1.63	93.2%	85%–96%
Boundary Coupling	11.85	3.07	74.1%	65%–82%

Note: Suppression rates are theoretical predictions under assumed decoupling efficiencies η. The ranges in the last column reflect a ±20% variation in η around their nominal values, as analysed in Section 5.3. These are not measured performance metrics.

The relatively low overall coupling suppression rate (49.4%) is primarily attributable to the non-decouplable nature of explicit coupling (with a suppression rate of 0%). This phenomenon is consistent with the architecture-preservation principle: explicit coupling constitutes a physical prerequisite for the system to achieve its intended functionality and should not be forcibly decoupled. Furthermore, the absence of detected positive feedback loops (0 loops) together with a network stability index of Ω = 1.000 jointly validate the stability of the architecture, while the 20 potential coupling warnings provide clear directions for further design optimization.

In summary, this case study demonstrates that the proposed coupling network framework is capable of: (1) inferring 20 high-confidence potential coupling paths based on known coupling records, thereby achieving a transition from "reactive response" to "proactive early warning"; (2) quantifying the theoretical suppression effects of implicit coupling (**93.2%**) and boundary coupling (74.1%); (3) validating architectural stability through positive feedback loop detection (0 loops) and the stability index Ω = 1.000; and (4) providing designers with structured decoupling decision-making recommendations, rather than replacing engineering judgment. The framework has been computationally verified, and its theoretical predictions are qualitatively consistent with published experimental trends reported in the literature for high-speed trains. Its potential for generalization to other complex electromechanical systems remains to be further investigated.

5. Theoretical Verification and Validation

To ensure methodological rigor, the proposed framework is subject to theoretical verification and validation. Verification confirms that the framework is implemented as specified; validation examines whether the framework addresses the intended design problem and whether its theoretical predictions are consistent with published engineering evidence. Because the contribution of this paper is theoretical and methodological, validation does not rely on hardware experiments or prototype testing. Instead, it proceeds through conceptual validation, external consistency checking, sensitivity analysis, boundary-condition and failure-mode analysis, and a list of falsifiable predictions. This section reports the verification and validation logic, cross-referencing the detailed results already presented in Sections 3 and 4.

5.1 Verification

Verification addresses the question: is the framework implemented correctly? It is performed at four levels.

Code and analytical cross-checking. The entire pipeline is implemented as open-source Python code structured to match L0–L5. Each mathematical formulation—residual coupling matrix R(Eq. 20–21), coupling elasticity matrix $\boldsymbol{X}$(Eq. 28), path degree d_p (Eq. 34), positive feedback criterion $X_{pq} \cdot X_{qp} > 0$ (Definition 15)—is implemented twice: once following the analytical formula, and once via an independent numerical procedure.

On **the small test graphs examined**, elasticity entries, path degrees, and feedback loop counts are manually verified against hand calculations. No discrepancies were found.

Numerical stability. The coupling elasticity matrix computation uses numerical differentiation with a relative perturbation step size of $\delta = 0.01$, where the absolute perturbation is $\Delta = \delta \cdot C_q$. Step-size sensitivity is checked by varying $\delta$from 0.001 to 0.05. **Coupling elasticity matrix entries**, path degrees, and P0–P3 rankings remain stable; maximum relative deviation is below 2%, with no rank reversals within the same priority tier. The numerical differentiation is therefore stable under the tested perturbation range.

Enumeration correctness. The CSP screening result (2,187 → 648 → 468) is cross-checked by an independent enumeration script that applies all constraints and compatibility rules directly, without using the inclusion–exclusion shortcut. Direct enumeration produces exactly the same result: 648 performance-feasible, 180 compatibility-excluded, 468 feasible. This confirms the inclusion–exclusion calculation $108 + 108 + 72 - (54 + 36 + 36) + 18 = 180$.

Degeneracy testing. The L1.5 inference layer is designed to reduce to L1 when no shared neighbors exist and physical-field overlap is zero. This degeneracy was tested by constructing synthetic coupling networks with no shared neighbors and

zero field overlap. In all test cases, the predicted latent coupling intensity B_{ij}^{pred} was identically zero, and the extended matrix B^{ext} reduced exactly to the known implicit coupling matrix B. This confirms that L1.5 is a strict extension of L1, not a substitute for it.

GNN training, test RMSEs, and network metric calculations are reported in Sections 4.3 and 4.7, respectively. Their consistency with the underlying formulations is verified by the independent implementation described above. Together, these checks confirm that the framework is implemented as specified. They are Type I verification activities, not validation activities, and are consistent with the methodological expectations for verification in design research [55].

5.2 Validation

Validation addresses the question: does the framework address the intended design problem? Because the contribution is theoretical and the problem definition is original, a direct quantitative benchmark against existing methods is not straightforward. Instead, validation is performed through conceptual validation, external consistency checking against published measurements, retrospective consistency checking against documented industrial cases, qualitative comparison with existing methods, decision-oriented validation, a formal expert assessment protocol, and a list of falsifiable predictions. This validation strategy is consistent with recent JED editorials on verification and validation [55], industrial relevance [53], rigorous problem formulation [54], and data-informed design [56].

5.2.1 Conceptual Validation: Problem Definition and Theoretical Consistency

The framework is derived from a clearly identified theoretical gap: Axiomatic Design (AD), as the most formalized function-centric design theory, lacks a representational slot for physical-field coupling and cannot generate decoupling components. FBS, TRIZ, and DSM share this limitation, but AD provides the most direct target for extension because its Independence Axiom explicitly claims that functional independence yields a valid architecture. Theorem 1 formalizes this gap as a representational incompleteness of AD: functional independence does not entail physical independence. The proposed dual-domain framework is a direct extension of AD, treating the functional domain and the physical-field domain as co-equal representational structures. The L0–L5 analysis chain operationalizes this dual-domain view, and each layer is logically consistent with the preceding one. The framework therefore satisfies the criteria of conceptual validation: it is grounded in a robust theoretical gap, it is applicable to the intended design stage (physical architecture synthesis), and it contributes a new representational mechanism—joint representation and recommendation of functional and decoupling components.

5.2.2 External Consistency with Published Measurements and Industrial Cases

The theoretically inferred coupling paths are compared with published bench-test and field-test data (Section 4.12.3). Shi et al. [46], Chi et al. [47], and Wang et al. [50] report vibration transmission paths through the secondary suspension, primary suspension, and bogie frame. These reported paths are qualitatively consistent with the paths that the L1.5 model infers from topological common neighbors.

To partially address industrial relevance, the framework was also retrospectively applied to three documented industrial cases. In each case, the L1.5 latent coupling inference and L4 priority ranking were examined to determine whether they could identify the coupling path that the original engineering teams addressed reactively.

(1) Shenzhou-5 POGO vibration. The framework would represent the launch vehicle structure and the propellant feed system as two functionally independent subsystems. The L1.5 inference would identify a latent coupling path between them through the shared fluid and mechanical fields, driven by pressure oscillation in the feed system and structural vibration of the launch vehicle. This inferred path corresponds exactly to the POGO coupling that the Shenzhou program later addressed, first by a parameter-level patch (Shenzhou-6, reduced bellows count) and then by a mechanism-level decoupling component (Shenzhou-7, variable-capacity accumulator). The framework's L4 ranking would assign this path a high priority, consistent with the severity of the incident.

(2) AMG magnetorheological mount. The framework would represent the powertrain and the car body as functionally independent subsystems. The L1.5 inference would identify a latent coupling path through the shared mechanical and vibration fields, driven by powertrain motion and structural vibration of the body. This inferred path corresponds to the coupling that the second-generation magnetorheological mount was designed to suppress, extending isolation from the 2–22 Hz range to the 30–150 Hz range. The L4 ranking would assign this path a high priority because it affects both low-frequency motion control and high-frequency noise attenuation.

(3) BMW hydraulic bushing. The framework would represent the suspension links and the subframe as functionally independent subsystems. The L1.5 inference would identify a latent coupling path through the shared mechanical and vibration

fields, driven by longitudinal and lateral wheel forces transmitted through the lower control arm. This inferred path corresponds to the coupling that the hydraulic bushing was introduced to suppress, isolating suspension vibration from the car body. The L4 ranking would assign this path a medium-to-high priority because it affects both force decoupling and ride comfort.

Across all three cases, the coupling path inferred by the framework and the decoupling component introduced by the engineering team correspond one-to-one. This is a retrospective consistency check against documented industrial practice, not a prospective validation. It is consistent with the call for industrial relevance in design research [53].

It should be emphasized that this is an external consistency check against published data, not an experimental validation conducted by the authors.

5.2.3 Qualitative Comparison with Existing Methods

The proposed framework is an extension of Axiomatic Design (AD), not a replacement. Original AD, based on the Independence Axiom, ensures FR–DP independence but does not guarantee field independence; it also has no representational slot for decoupling components. The proposed dual-domain extension retains the FR–DP mapping of AD while adding a physical-field domain, thereby enabling the representation and generation of decoupling components.

The extended framework is compared qualitatively against four external baselines: DSM-based partitioning (identifies module boundaries but not decoupling components), rule-based configuration (compatibility constraints without physical-field representation), pure simulation (requires a complete system model and cannot represent implicit coupling), and linear regression (cannot capture nonlinear cross-terms). The original AD Independence Axiom is treated as the theoretical starting point that the present work extends, rather than as an external baseline.

To our knowledge, the extended framework is the only approach that addresses explicit, implicit, and boundary coupling within a unified architecture generation process and that can recommend decoupling components as design objects. A quantitative comparison with the external baselines is left as future work.

5.2.4 Decision-Oriented Validation

While the preceding assessments address whether the framework produces theoretically consistent outputs, an additional question remains: whether the framework supports the intended design decisions in a meaningful way. This subsection examines the decision context, the consequences of missing critical couplings, the contrast with existing design workflows, and the mapping between stakeholder needs and framework outputs. It is a conceptual validation based on engineering roles, published industrial cases, and the structure of the case study, not an empirical validation based on stakeholder interviews or enterprise project data. This decision-oriented perspective is consistent with the JED editorials on industrial relevance [53] and data-informed design [56].

Decision context and stakeholders. The framework is intended for use during the physical architecture synthesis stage of complex electromechanical products, where system architects and overall design engineers must decide which functional components to select and whether dedicated decoupling components are required. In the high-speed train case, the relevant stakeholders include the system architect, the bogie and car-body design engineers, and the NVH engineer. Their shared decision problem is to identify, before integration, which physical-field couplings are likely to cause vibration, noise, or stability problems, and how to prioritize mitigation measures under limited design resources. The framework addresses this context by producing a ranked list of coupling paths (P0–P3) and matching decoupling component recommendations, rather than leaving these decisions to post-hoc measurement or field observation.

Consequences of missing critical couplings. The framework's value depends not only on what it identifies but also on the consequences of failing to address what it flags. In the high-speed train case, the P0 boundary couplings (e.g., B02–RAIL, AIR–P05) involve wheel–rail and pantograph–catenary interfaces that directly affect safety and operational reliability; if these are neglected, external disturbances cannot be sufficiently attenuated, and ride comfort or current collection quality may degrade. The P1 category, although empty in this case, represents positive feedback loops that could lead to self-amplifying instability if present. The P2 high-path-degree couplings (e.g., N03–R01) involve cross-subsystem timing or longitudinal dynamics; ignoring them may cause control-loop conflicts or coupler-area dynamic problems. By assigning priority labels and recommending decoupling components, the framework provides evidence provides evidence **consistent with** the severity of these potential consequences.

Comparison with existing design workflows. In conventional design workflows, implicit couplings are typically discovered only after integration, through vehicle NVH measurements, field tests, or operational incidents—as illustrated by the Shenzhou-5 POGO vibration case and the automotive NVH examples discussed in Section 1. The proposed framework shifts this discovery to the architecture synthesis stage, where design freedom is still high and changes are less costly. This early-warning capability does

not replace experimental validation, but it provides a structured basis for design decisions that would otherwise rely on engineering intuition or late-stage testing.

Stakeholder needs mapping. The framework maps to stakeholder needs as follows. For system architects, it provides a system-level coupling network and P0–P3 priority ranking to guide architecture selection. For subsystem engineers, it identifies specific coupling paths and recommended decoupling component types (e.g., timing contracts, aerodynamic fairings, axle box isolation). For NVH engineers, it highlights vibration and acoustic transmission paths that may require isolation or damping. For project managers, it supports resource allocation by concentrating attention on high-risk paths. These mappings are derived from engineering roles and decision scenarios implicit in the case study and published industrial practice. They constitute a decision-oriented validation argument, not an empirical validation.

5.2.5 Falsifiable Predictions and Boundary Conditions

The framework yields a set of falsifiable predictions that can be tested in future experimental or field studies:

1. The 20 high-risk latent coupling paths inferred at L1.5 (Section 4.8) should be physically verifiable through targeted bench or field measurements. If a substantial number of these paths are shown to be absent under normal operating conditions, the L1.5 inference logic would require revision.
2. The P0 boundary couplings (e.g., B02–RAIL, AIR–P05) are predicted to be the dominant residual coupling sources after decoupling. If experimental measurements show that other paths dominate, the priority ranking would need recalibration.
3. The network stability index $\Omega = 1.000$ predicts the absence of self-amplifying coupling cycles. If a positive feedback loop is experimentally identified in the current architecture, the stability conclusion would be challenged.

The framework also has identifiable boundary conditions. When no shared neighbors exist and physical-field overlap is zero, L1.5 degenerates to L1, and the framework reverts to the conventional known-coupling model. When the candidate space exceeds exhaustive enumeration capacity, the CSP–GNN–Pareto pipeline must be replaced by heuristic search, which may affect the completeness of the Pareto frontier. These boundary conditions delimit the scope within which the framework's conclusions hold. This formulation of testable claims is consistent with the JED editorial on rigorous problem formulation [54].

5.2.6 Expert Assessment Protocol (Future Work)

A formal expert assessment protocol has been designed to evaluate the engineering plausibility of the L1.5 inferred paths and the L5 decoupling recommendations. The protocol involves 3–5 domain experts in high-speed train dynamics and NVH. Each expert will rate each inferred coupling path and recommended decoupling component on a 5-point Likert scale for (i) physical plausibility, (ii) engineering relevance, and (iii) implementability. The ratings will be aggregated to assess expert agreement. Because the present study is theoretical and computational, the execution of this protocol is identified as immediate future work, in line with the methodological expectations of design research [55].

5.3 Sensitivity and Robustness Analysis

Sensitivity analysis is a validation activity: it examines whether the framework's conclusions are robust to parameter uncertainty, without claiming experimental validation. The framework contains several configurable engineering parameters. To assess whether the main conclusions are robust to their values, a sensitivity analysis was performed on four parameter groups: decoupling efficiency η, similarity weights α, β, γ, latent coupling threshold θ_{latent}, and priority weights w_1, w_2, w_3. The analysis examines three outputs: (i) the P0–P3 priority ranking, (ii) the network stability index Ω, and (iii) the number of inferred latent coupling paths and the resulting decoupling recommendations. All sensitivity runs use the same 67-node, 90-edge coupling network and the same 468 feasible architectures; only the parameter under study is varied.

5.3.1 Sensitivity to Decoupling Efficiency $\boldsymbol{\eta}$

$\eta$was varied by ±10% and ±20% around its default values for all coupling types. Across all runs, the P0 classification (boundary couplings involving RAIL, AIR, or CAT) remained unchanged, and no rank reversal occurred within the same priority tier. The network stability index remained $\Omega = 1.000$, and the number of non-zero elements in the residual matrix Rchanged by less than 4%. The total coupling suppression rate varied within ±3.5 percentage points. These results indicate that the P0 classification and the stability conclusion are robust to moderate uncertainty in η.

5.3.2 Sensitivity to Similarity Weights $\boldsymbol{\alpha, \beta, \gamma}$

Three alternative weight sets were tested: (0.5, 0.4, 0.1), (0.7, 0.2, 0.1), and the default (0.6, 0.3, 0.1). The number of high-risk latent coupling paths ($B_{\text{pred}} > \theta_{\text{latent}}$) varied between 17 and 23, compared with the default 20. The top five predicted paths remained the same in all runs; only their ordering changed slightly. The highest-ranked path C01 ↔ B02 remained first in all configurations. This indicates that the L1.5 inference is qualitatively stable under reasonable variations of α, β, γ.

5.3.3 Sensitivity to Latent Coupling Threshold $\boldsymbol{\theta}_{\text{latent}}$

$\theta_{\text{latent}}$was varied from 0.10 to 0.20 in increments of 0.02. The number of inferred latent coupling paths decreased monotonically from 31 ($\theta_{\text{latent}} = 0.10$) to 12 ($\theta_{\text{latent}} = 0.20$), with the default value 0.15 yielding 20 paths. The top-ranked path C01 ↔ B02 remained above threshold across the entire range. This confirms that θ_{latent}functions as a sensitivity-control parameter, allowing designers to trade off between coverage and false positives without altering the underlying inference logic.

5.3.4 Sensitivity to Priority Weights $\boldsymbol{w_1, w_2, w_3}$

The priority weights in Eq. (40) were varied across three configurations: (0.5, 0.3, 0.2) default, (0.6, 0.3, 0.1), and (0.4, 0.4, 0.2). The set of P0 paths remained identical in all runs. The P2 ranking changed in order but not in membership. No path moved from P0 to P2 or vice versa. This indicates that the priority classification is robust to moderate changes in w_1, w_2, w_3.

5.3.5 Summary

Across all four parameter groups, the P0 classification, the network stability conclusion ($\Omega = 1.000$), and the identity of the highest-ranked latent coupling path (C01 ↔ B02) remained unchanged. Parameter variations affect numerical values and secondary rankings, but not the theoretical validity or the main engineering conclusions of the framework. Detailed numerical results are provided in Appendix Table A9.

5.4 Limitations

The framework's limitations are fourfold.

Engineering priors. Decoupling efficiencies η and priority weights are engineering priors, not experimentally measured values. Sensitivity analysis (Section 5.3) shows that the P0 classification is robust to ±10% variations in η, but all suppression rates remain theoretical predictions under assumed decoupling efficiencies. Future work should replace these priors with experimentally validated efficiencies.

Combinatorial scaling. Exhaustive enumeration (3^7 = 2187) applies to small-to-medium problems. Larger candidate spaces require heuristic search. The framework is agnostic to the search method; CSP–GNN–Pareto can be replaced by any efficient strategy without altering the theoretical foundation.

Engineering implementation validation. The present study is theoretical and computational. Hardware-in-the-loop and prototype testing are outside the scope of this paper, because the contribution is a representational extension of **Axiomatic Design** rather than an engineering implementation. Future work may evaluate the deviation between theoretical and actual decoupling efficiencies on real prototypes; this would test the engineering applicability of the framework, not its theoretical validity.

Decision-oriented validation. The decision-oriented validation in Section 5.2 is based on engineering roles, published industrial cases, and the structure of the case study. It is a conceptual validation, not an empirical validation. Empirical validation against real-world design projects remains future work.

All suppression rates reported in this paper are theoretical predictions under assumed decoupling efficiencies, not measured values.

The complete code for all computational components described in this paper, including the dual-domain mapping framework, CSP screening, the GNN surrogate model, Pareto optimization, and the L0–L5 coupling analysis pipeline, is openly available at https://github.com/lijingp/high_speed_train_coupling_analysis-v4.2.py.

6. Discussion

6.1 Credibility and Theoretical Value of L1.5 Latent Coupling Inference

The inference results generated by the L1.5 layer should not be interpreted as "deterministic detections," but rather as "probabilistic early warnings." Their value lies in directing designers' attention toward high-risk regions, rather than in providing indisputable conclusions. Because the contribution of this paper is theoretical, the credibility of the inference results is established through the following mechanisms:

Engineering interpretability. Each predicted path can be traced back to its inferential basis (shared neighbors, shared physical fields) and is consistent with engineering intuition. For instance, the predicted strength for C01–B02 reaches 0.992, on the basis of three common-cause neighbors (B01 bogie frame, B03 primary suspension, B05 traction motor) and three shared physical fields (vibration, acoustics, mechanics). Physically, although no direct interface between the car body and the wheelset is documented, a vibration transmission pathway inevitably exists through the suspension system—the framework successfully quantifies this "engineering common sense" into a computable metric.

Graceful degradation as a verification property. When the inference conditions are not satisfied (i.e., no common neighbors, no overlapping physical fields), L1.5 smoothly degrades to L1, thereby avoiding the generation of spurious warnings and ensuring the robustness of the framework across varying degrees of information completeness.

Controllable threshold. Designers can adjust $\theta_{\text{latent}}$to control the sensitivity of the early-warning mechanism: raising the threshold reduces false positives, while lowering it increases coverage, thereby accommodating the requirements of different engineering scenarios.

The incorporation of L1.5 upgrades the entire framework from a closed loop of "known → known" to an open loop of "known → inferred → warned → validated." This constitutes **a distinguishing feature** that separates the proposed framework from traditional DSM-based approaches and existing modularization studies—it not only informs the designer of "the current state of the system," but also of "where problems may potentially arise."

Nevertheless, it must be acknowledged that the inference results of L1.5 are fundamentally based on statistical inference derived from network topology and physical-field labels, rather than from measured data. The predictive confidence of these results is fundamentally constrained by the completeness of the known coupling network—if the initial design documentation itself omits a substantial number of couplings, the baseline network underlying the inference will be incomplete, and the resulting predictions may consequently be biased. Hardware experiments and field testing are outside the scope of this theoretical study; they are identified as future work for engineering implementation, not as a requirement for the theoretical validity of the framework.

6.2 Consistency with Advanced Industrial Decoupling Practice

The decoupling logic proposed in this paper is consistent with advanced industrial practices: adaptive suspension systems in automotive engineering decouple road excitation from body response; variable-energy accumulators in aerospace sever positive feedback loops at the source; and standardized power and communication interfaces in rail transit enable platform-level modular decoupling. These industrial cases establish the existence of the design gap; they are not used to validate the proposed framework experimentally.

6.3 Scope and Boundary Conditions

The proposed method is subject to the following scope and boundary conditions.

First, the parameters of candidate solutions and decoupling efficiencies depend on engineering experience (preset ηvalues in the L1 knowledge base). Although Section 4.12.3 evaluates the theoretical benefits through formula derivation (e.g., residual decreasing from 0.200 to 0.040), this constitutes theoretical evaluation within the scope of the present study. Hardware-in-the-loop testing and prototype measurement would test the engineering applicability of the framework, not its theoretical validity.

Second, the exhaustive enumeration ($3^7 = 2187$ combinations) is applicable only to small- to medium-scale problems. As the number of subsystems increases or the candidate space grows exponentially, heuristic search methods (e.g., genetic algorithms, Bayesian optimization) would be needed as alternatives.

Third, full-scale physical experiments on high-speed trains are outside the scope of this theoretical study. Transitioning from theoretical derivation to engineering implementation would require evaluating the deviation between actual and theoretical decoupling efficiencies on real prototypes or hardware-in-the-loop simulation platforms; this is identified as future engineering work.

6.4 Implications for Design Cognition

The four-category classification of implicit coupling provides a cognitive scaffold for identifying physical-field interactions that remain invisible within functional decomposition. By rendering explicit what would otherwise remain hidden until failure occurs, this framework suggests that design education and practice could benefit from explicit training in physical-field awareness, and that design tools should provide visualization and reasoning support for field interactions beyond mere functional reasoning.

7. Conclusions

This paper establishes a dual-domain extension of Axiomatic Design (AD) for physical architecture design. Its theoretical foundation is Theorem 1: the Independence Axiom of AD is necessary but not sufficient for system integrability, because it cannot represent physical-field interactions between functionally independent components. Consequently, any function-centric mapping such as AD's FR–DP mapping outputs functional components C_{func}, but systematically omits the decoupling components C_{dec}required to suppress field interactions Ψ_{ij}. The L0–L5 coupling network analysis framework proposed in this paper provides a systematic representational response to this incompleteness, through the identification, quantification, and prioritization of coupling paths.

The core theoretical contribution is a representational extension of AD: the Independence Axiom is necessary but not sufficient, because AD has no representational slot for physical-field coupling or for components that realize no functional

requirement. The methodological contribution is a coupling network analysis and decoupling decision-making framework based on complex network theory, which abstracts system components and their coupling relationships into an undirected weighted graph $G = \{V, E, R\}$, where nodes represent functional components and boundary nodes, edges represent coupling relationships, and edge weights are quantified by the residual coupling matrix R. Building upon this, a **coupling elasticity matrix** $X$is constructed to capture higher-order interactions among paths, with the path degree $d_p = \sum_{q \neq p} |X_{pq}|$defined to quantify the influence of a given path, and positive feedback loops detected via the condition $X_{pq} \cdot X_{qp} > 0$. Finally, priority labels ranging from P0 to P3 are assigned based on a comprehensive consideration of residual strength, path degree, and positive feedback loop risk, generating an ordered list of decoupling targets.

This method provides **traceable decision support**—each recommendation can be traced back to explicit mathematical criteria, enabling designers to understand the reasoning chain behind each recommendation without relying on black-box models.

(1) The complex network approach reveals the topological structure and propagation patterns of the coupling network, and is used to illustrate the selection of an optimal architecture in the computational demonstration. In the high-speed train demonstration, CSP screening and Pareto multi-objective optimization identified a reference architecture from 2,187 combinations (cost 3.25 million CNY, braking distance 5,050 m). A coupling network comprising 67 nodes and 90 edges was constructed, exhibiting a network density of 0.0407, indicative of a sparse structure. Hub node identification revealed that B02 (wheel set) ranks at the center of the network with a degree of 12, followed by R01 (BCU) and N04 (train bus) with degrees of 11, **thereby identifying candidate critical pathways** of coupling propagation. The residual matrix heatmap shows that the 180 non-zero elements are primarily distributed in the crossings between boundary nodes and internal components, with the external boundaries (e.g., B02–RAIL, residual 0.285; AIR–P05, residual 0.225) constituting the principal sources of residual coupling. These results are illustrative, not an industrial validation.

(2) The coupling elasticity matrix analysis reveals higher-order interactions among coupling paths. The results of the six-subspace decomposition show that the Frobenius norms of the explicit, implicit, and boundary coupling categories are all equal to 9.75, indicating that the three categories of coupling are balanced in terms of interaction strength, and that neglecting any one of them would render the analysis incomplete. No positive feedback loops were detected (0 loops), and the network stability index $\Omega = 1.000$, indicating the absence of self-amplifying coupling cycles within the system.

(3) The network analysis results are translated into a structured decoupling priority list, illustrating the theoretical feasibility of the dual-domain framework in generating decoupling components. The L1.5 latent coupling inference identified 20 potential paths from the known couplings, with the highest strength reaching 0.992 (C01–B02), thereby achieving a transition from “reactive response” to “proactive early warning.” The L4 priority ranking classified the paths into four levels, P0–P3, and the L5 layer output three actionable recommendations, matching specific decoupling components to critical paths based on the knowledge base (e.g., Timing Contract for N03–R01). The theoretical re-evaluation based on the residual update formula shows that, following the implementation of the decoupling component, the residual for this path decreased from 0.200 to 0.040, supporting the theoretical feasibility of the framework in coupling suppression. Furthermore, the computational results based on the residual matrix show that the implicit coupling residual decreased from 24.10 to 1.63 (a theoretical suppression rate of 93.2%), and the boundary coupling residual decreased from 11.85 to 3.07 (a theoretical suppression rate of 74.1%). All suppression rates reported in this paper are theoretical predictions under assumed decoupling efficiencies, not measured values.

Because the contribution of this paper is theoretical and methodological, the following are identified as future work for engineering implementation and theoretical extension: (1) engineering implementation validation through hardware experiments and field testing, to assess the deviation between theoretical and actual decoupling efficiencies; (2) developing an automated decoupling component library and retrieval system to reduce reliance on expert experience; (3) extending the framework to comparative coupling network analysis across multiple solutions on the Pareto front; and (4) exploring the application of the framework in domains such as aerospace and marine engineering, to assess its cross-domain transferability.

AI Tool Usage Statement

During the writing of this article, we utilized the generative artificial intelligence tool Claude (version: 3.5 Sonnet) solely for polishing and correcting the language expression of the English manuscript to enhance the readability and fluency of the text. All scientific content, data, analysis, conclusions, and final modifications were independently completed by the author. The AI tool did not participate in the research design, data generation, or core argumentation. After its use, the author has reviewed all the content

sentence by sentence and assumes full responsibility for it.

Data Availability Statement: All code and data are available at https://github.com/lijingp/high_speed_train_coupling_analysis-v4.2.py.

Conflict of Interest Statement: The authors declare no competing interests.

The entire work was conceived, investigated, and drafted by the first author, who also performed the calculations. The second author provided guidance and oversight

No funding was received for this study.

References

[1] Chen L, et al. Automated physical architecture generation and evaluation using dynamic programming and TOPSIS[J]. Journal of Engineering Design, 2019, 30(5): 287-310.

[2] Wang, R., Wei, Z., Li, H., Wang, Z., Huang, Y., & Wang, G. (2025). Intelligent design exploration method for complex engineered system architecture generation. *Journal of Engineering Design*, *36*(5-6), 797-835.

[3] Huang Z, et al. Knowledge graph-enabled functional-component matching and closed-loop simulation for physical architecture design[J]. Computers in Industry, 2025a, 156: 104072.

[4] Huang Z, et al. Integrating case-based knowledge with reinforcement learning for product configuration optimization[J]. Journal of Intelligent Manufacturing, 2024b, 35(4): 1823-1842.

[5] Zhang Y, et al. MBSE-based system modeling for requirement management and multi-view collaboration in complex product development[J]. Systems Engineering, 2022, 25(3): 245-262.

[6] Huang Z, Wang G, Yan Y, Li Z, Wei Z, Liu Z. Systematic design space exploration using morphological matrix, constraint satisfaction problem, evolutionary algorithm and improved TOPSIS[J]. Research in Engineering Design, 2024, 35(2): 189-212.

[7] Jing, L., Wang, J., Xie, J., Feng, D., Wang, J., Peng, X., & Jiang, S. (2022). A quantitative simulation-based conceptual design evaluation approach integrating bond graph and rough VIKOR under uncertainty. *Journal of Cleaner Production*, *380*, 134928.

[8] Pradas Gómez, A., Panarotto, M., & Isaksson, O. (2025). FUSE: A Novel Design Space Exploration Method for Aero Engine Components That Combines Functional and Physical Domains. *Aerospace*, *12*(1), 51.

[9] Isaksson, O., Wynn, D. C., & Eckert, C. (2023). Design perspectives, theories, and processes for engineering systems design. In *Handbook of engineering systems design* (pp. 1-47). Cham: Springer International Publishing.

[10] Gero J S. Design prototypes: A knowledge representation schema for design[J]. AI Magazine, 1990, 11(4): 26-36.

[11] Gero J S, Kannengiesser U. The situated function–behaviour–structure framework[J]. Design Studies, 2004, 25(4): 373-391.

[12] Dorst K, Vermaas P E. John Gero's Function-Behaviour-Structure model of designing: a critical analysis[J]. Research in Engineering Design, 2005, 16(1-2): 1-18.

[13] Altshuller, G. S. The Innovation Algorithm: TRIZ, Systematic Innovation and Technical Creativity[M]. Worcester, MA: Technical Innovation Center, 1999.

[14] Sheu D D, Chiu M C, Cayard D. The 7 pillars of TRIZ philosophies[J]. Computers & Industrial Engineering, 2020, 146: 106572.

[15] Yehya M I, Coulibaly A, Chibane H, et al. Framework for evaluating solution concepts in TRIZ based inventive designs using a functional, behavioral, and structural modeling approach[J]. FME Transactions, 2023, 51(4): 521-531.

[16] Sadeghi L, Dantan J Y, Mathieu L, et al. A design approach for safety based on Product-Service Systems and Function-Behavior-Structure[J]. CIRP Journal of Manufacturing Science and Technology, 2017, 19: 191-204.

[17] Shi H B, Huang D, Wang L, et al. An information integration approach to spacecraft fault diagnosis[J]. Enterprise Information Systems, 2021, 15(8): 1128-1161.

[18] Liu, S., Nan, S., & Tian, L. (2025). An Evaluation Method for the Skeleton Model Based on Function–Behavior–Structure Correlation Analysis. Machines, 13(1), 32. https://doi.org/10.3390/machines13010032

[19] Zhuang W, Lv X, Wu X, et al. An Agentic AI-Empowered product family configuration approach for personalizing rehabilitation assistive devices with Multi-faceted wearing experience[J]. Advanced Engineering Informatics, 2026, 74: 104695.

[20] Chen R R, Liu Y S, Cao Y, et al. ArchME: A Systems Modeling Language extension for mechatronic system architecture modeling[J]. Artificial Intelligence for Engineering Design, Analysis and Manufacturing, 2018, 32(1): 75-91.

[21] Huang H Z, Li Y, Liu W, Liu Y, Wang Z. Evaluation and decision of products conceptual design schemes based on customer requirements[J]. Journal of Mechanical Science and Technology, 2011, 25(9): 2413-2425.

[22] Huang Y, Wang G, Wang R, Wei Z, Liu Z, Yan Y. Architectural design space exploration of complex engineered systems with management constraints and preferences[J]. Journal of Engineering Design, 2024, 35(6): 743-774.

[23] Xu H, Yang L. Research on Module Division of Commercial Aircraft Based on Analytic Hierarchy Process and Gray Fuzzy Comprehensive Evaluation[J]. Aerospace, 2025, 12(6): 485.

[24] Zhu G N. Design concept evaluation considering information reliability, uncertainty, and subjectivity: An integrated rough-Z-number-enhanced MCGDM methodology[J]. Advanced Engineering Informatics, 2022, 54: 101796.

[25] Jiang, S., Dou, Y., He, S., Tan, B., Peng, X., & Jing, L. (2022). Fuzzy concept evaluation based on prospect theory and heterogeneous evaluation information. Journal of Computing and Information Science in Engineering, 22(4), 041003.

[26] Kamran, M., Salamat, N., Jana, C., & Xin, Q. (2025). Decision-making technique with neutrosophic Z-rough set approach for sustainable industry evaluation using sine trigonometric operators. *Applied Soft Computing*, *169*, 112539.

[27] Yang Y, Tian H, Loiseau J J, et al. Product Design Evaluation Method Using Consensus Measurement, Network Analysis, and AHP[J]. Mathematical Problems in Engineering, 2019, 2019: 1-9.

[28] Kulak O, Cebi S, Kahraman C. Applications of axiomatic design principles: A literature review[J]. Expert Systems with Applications, 2010, 37(9): 6705-6717.

[29] Wölfle, R., Saur-Amaral, I., & Teixeira, L. (2025). Case-Based Axiomatic Design Assistant (CADA): Combining Axiomatic Design and Case-Based Reasoning to Create a Design Knowledge Graph for Pharmaceutical Engineering. Applied Sciences, 15(3), 1467.

[30] Li, J., Wu, X., Zhang, X., Song, Z., & Li, W. (2022). Design of distributed hybrid electric tractor based on axiomatic design and Extenics. Advanced Engineering Informatics, 54, 101765.

[31] Kannan G, Noorul Haq A, Devika M. Fuzzy axiomatic design approach based green supplier selection: a case study from Singapore[J]. Journal of Cleaner Production, 2014, 96: 194-208.

[32] Cebi S, Celik M, Kahraman C. Structuring ship design project approval mechanism towards installation of operator–system interfaces via fuzzy axiomatic design principles[J]. Information Sciences, 2010, 180(6): 886-895.

[33] Fazeli H R, Peng Q. Generation and evaluation of product concepts by integrating extended axiomatic design, quality function deployment and design structure matrix[J]. Advanced Engineering Informatics, 2022, 54: 101716.

[34] Zheng, P., & Xie, S. Q. (2015, December). A rough set based fuzzy axiomatic design approach in evaluating customer-centric design alternatives. In 2015 IEEE International Conference on Industrial Engineering and Engineering Management (IEEM) (pp. 544-548). IEEE.

[35] Tan, S., Zhao, W., Liu, J., & Mao, Y. (2023). Adaptive control design for active Pogo suppression of large strap-on liquid launch vehicles. Acta Astronautica, 206, 43-56.

[36] Deb, K., Pratap, A., Agarwal, S., & Meyarivan, T. A. M. T. (2002). A fast and elitist multi-objective genetic algorithm: NSGA-II. IEEE transactions on evolutionary computation, 6(2), 182-197.

[37] Steffensen, R., Steinert, A., & Holzapfel, F. (2023). Incremental control as an enhanced and robust implementation of gain scheduled controllers avoiding hidden coupling terms. Aerospace Science and Technology, 141, 108500.

[38] Huynh, S., Cai, Y., Song, Y., & Sullivan, K. (2008, May). Automatic modularity conformance checking. In Proceedings of the 30th international Conference on Software Engineering (pp. 411-420).

[39] Li, J., Ding, G. (2026). Rethinking modular decomposition: A design-theoretic framework for managing explicit and implicit coupling in complex systems. *Journal of Mechanical Design*, under review. (Manuscript ID: 6848028).

[40] Peng, C., Zhang, Z., Liu, W., & Li, D. (2022). Ranking of Key Components of CNC Machine Tools Based on Complex Network. *Mathematical Problems in Engineering*, *2022*(1), 6031626.

[41] Xia, Y., Yang, N., Wang, H., Wang, X., Cui, M., & Li, M. (2023). Failure propagation prediction of complex electromechanical systems based on interdependence. *Electronics*, *12*(12), 2600.

[42] Lin, S., Jia, L., Zhang, H., & Zhang, P. (2022). Network approach to modelling and analysing failure propagation in high-speed train systems. *International Journal of Systems Science: Operations & Logistics*, *9*(4), 529-545.

[43] Ladyman, J., Lambert, J., & Wiesner, K. (2013). What is a complex system?. *European Journal for Philosophy of Science*, *3*(1), 33-67.

[44] Mahabadi, Z., Varga, L., & Dolan, T. (2023). A survey of multilayer networks modelled to assess robustness in infrastructure systems. *Proceedings of the Institution of Civil Engineers-Smart Infrastructure and Construction*, *176*(3), 117-125.

[45] Aleta, A., Teixeira, A. S., Ferraz de Arruda, G., Baronchelli, A., Barrat, A., Kertész, J., ... & Fortunato, S. (2026). Multilayer network science: theory, methods, and applications. *Journal of Complex Networks*, *14*(2), cnag007.

[46] Shi H., Zeng J., Duan L. Carbody swaying suppression for a high-speed rail vehicle by utilising active lateral suspension control[J]. Vehicle System Dynamics, 2025, 63(10): 1998-2017.

[47] Chi, C., Chang, C., Liang, S., et al. Research on the application of switch-type anti-yaw dampers in high-speed trains[J]. Journal of the China Railway Society, 2025, 47(2). (in Chinese)

[48] Wan S., Song L., Hu X., et al. Design and static and dynamic analysis of floor vibration isolators for high-speed train[J]. Science Progress, 2024, 107(4).

[49] Sun Y., Zhou J., Gong D., et al. Vibration control of high-speed trains self-excitation under-chassis equipment by HSLDS vibration isolators[J]. Journal of Mechanical Science and Technology, 2019, 33(1): 65-76.

[50] Wang Q., Xiao X., Han J., et al. Vehicle modelling for high-frequency vibration transmission through primary suspensions[J]. Vehicle System Dynamics, 2026, 64(3): 568-610.

[51] Xia Z., Gong D., Zhou J., et al. Decoupling optimization design of under-chassis equipment suspension system in high-speed trains[J]. Shock and Vibration, 2018, 2018: 6292595.

[52] Jin, M., Hu, M., Li, H., Yang, Y., Liu, W., Fang, Q., & Liu, S. (2022). Experimental Study on the Transient Disturbance Characteristics and Influence Factors of Pantograph–Catenary Discharge. Energies, 15(16), 5959. https://doi.org/10.3390/en15165959

[53] Jiao, R. (2026). Context matters: reasserting industrial relevance in design research–why design research cannot be self–contained. *Journal of Engineering Design*, *37*(3), 583-589.

[54] Jiao, R. (2026). Towards rigorous problem formulation for engineering design research: from motivations to measurable claims via metric-measure-method. *Journal of Engineering Design*, *37*(6), 2145-2171.

[55] Jiao, R. (2026). Demystifying verification and validation in design research methodology–from underdeveloped practice to methodological rigour. *Journal of Engineering Design*, *37*(4), 1143-1162.

[56] Jiao, R. (2026). From ‘data-driven’to ‘data-informed’design—grounding AI for design in knowledge, context and decisions. *Journal of Engineering Design*, *37*(5), 1753-1775.

Supplementary Files

This is a list of supplementary files associated with this preprint. Click to download.

- Appendix1017.docx